Gravitational form factors of the proton from lattice QCD

Daniel C. Hackett,[1, 2] Dimitra A. Pefkou,[3, 2] and Phiala E. Shanahan[2]

[1]*Fermi National Accelerator Laboratory, Batavia, IL 60510, U.S.A.*
[2]*Center for Theoretical Physics, Massachusetts Institute of Technology, Cambridge, MA 02139, U.S.A.*
[3]*Department of Physics, University of California, Berkeley, CA 94720, U.S.A*

The gravitational form factors (GFFs) of a hadron encode fundamental aspects of its structure, including its shape and size as defined from e.g., its energy density. This work presents a determination of the flavor decomposition of the GFFs of the proton from lattice QCD, in the kinematic region $0 \leq -t \leq 2$ GeV^2. The decomposition into up-, down-, strange-quark, and gluon contributions provides first-principles constraints on the role of each constituent in generating key proton structure observables, such as its mechanical radius, mass radius, and D-term.

Achieving a quantitative description of the structure of the proton and other hadrons in terms of their quark and gluon constituents is a defining challenge for hadronic physics research. The gravitational structure of the proton, encoded in its gravitational form factors (GFFs), has come under particular investigation [1–23] since the first extraction of one of its GFFs from experimental measurements in 2018 [24]. Defined from the matrix elements of the energy-momentum tensor (EMT) in a hadron state, GFFs describe fundamental properties such as the mass and spin of a state, the less well-known but equally fundamental D-term (or "Druck" term), and information that can be interpreted in terms of the distributions of energy, angular momentum, and various mechanical properties of the system [25–28].

The proton GFFs $A(t)$, $J(t)$, and $D(t)$ are defined as

$$\langle N(\mathbf{p}', s')| \hat{T}^{\mu\nu} |N(\mathbf{p}, s)\rangle = \frac{1}{m}\bar{u}(\mathbf{p}', s')\Big[P^\mu P^\nu A(t)+$$
$$iP^{\{\mu}\sigma^{\nu\}\rho}\Delta_\rho J(t) + \frac{1}{4}(\Delta^\mu \Delta^\nu - g^{\mu\nu}\Delta^2)D(t)\Big]u(\mathbf{p}, s), \quad (1)$$

where $a^{\{\mu}b^{\nu\}} = (a^\mu b^\nu + a^\nu b^\mu)/2$, $N(\mathbf{p}, s)$ is a proton state with three-momentum $\mathbf{p}$ and spin eigenvalue $s = \pm\frac{1}{2}$, $u(\mathbf{p}, s)$ is the Dirac spinor, $P = (p + p')/2$, $\Delta = p' - p$, $t = \Delta^2$, and $\sigma_{\mu\nu} = \frac{i}{2}[\gamma_\mu, \gamma_\nu]$ where γ_μ are the Dirac matrices. $\hat{T}^{\mu\nu}$ is the renormalization-scale independent [29] symmetric EMT of QCD [30]. It can be decomposed into quark and gluon contributions as $\hat{T}^{\mu\nu} = \sum_{i\in\{q,g\}} \hat{T}_i^{\mu\nu}$, where

$$\hat{T}_g^{\mu\nu} = 2\,\text{Tr}\left[-F^{\mu\alpha}F^\nu_{\ \alpha} + \frac{1}{4}g^{\mu\nu}F^{\alpha\beta}F_{\alpha\beta}\right],$$
$$\hat{T}_q^{\mu\nu} = \sum_f \left[i\bar{\psi}_f D^{\{\mu}\gamma^{\nu\}}\psi_f\right], \quad (2)$$

$F^{\mu\alpha}$ is the gluon field strength tensor, ψ_f is a quark field of flavor f, and $D^\mu = \partial^\mu + igA^\mu$ is the covariant derivative. The matrix elements of $\hat{T}_i^{\mu\nu}$ define the renormalization scheme- and scale-dependent partonic contributions to the GFFs. The corresponding forward limits $A_i(0)$, $J_i(0)$, and $D_i(0)$ describe the partonic decomposition of the proton's momentum, spin, and D-term, respectively. Poincaré symmetry imposes the sum

rules [8, 31–34] $A(0) = 1$ and $J(0) = 1/2$, while the value of $D(0)$ is conserved but not constrained from spacetime symmetries [35]. The t-dependence of the GFFs encodes additional information about the quark and gluon contributions to densities in the proton [25–27, 36]. While determination of the flavor decomposition of the proton's momentum and spin have a long history, reviewed in Refs. [37–39], constraints on the D-term [17–20, 24, 40, 41] and the t-dependence [17–21, 41–43] of the proton's GFFs have been comparatively recent.

This work presents a flavor-decomposition of the total GFFs of the proton, $A(t)$, $J(t)$, and $D(t)$, into gluon, up-, down-, and strange-quark contributions, achieved through a lattice QCD calculation with quark masses yielding a close-to-physical value of the pion mass. The $D_{u+d}(t)$ and $D_g(t)$ GFFs are found to be consistent with the recent experimental extractions of these quantities [24, 40], while the t-dependence of $A_g(t)$ is consistent with one of the two analyses of experimental data presented in Ref. [40] and in tension with the other (including the updated analysis of Ref. [44]). The individual up-, down-, and strange-quark GFFs are quantified for the first time from experiment or first-principles theory. From the GFFs, the energy and radial force densities of the proton, and the associated mass and mechanical radii, are computed, allowing a quantitative comparison of these different measures of the proton's size.

Lattice QCD calculation: The lattice QCD calculation is performed using a single ensemble of gauge field configurations generated by the JLab/LANL/MIT/WM groups [45], using the Lüscher-Weisz gauge action [46] and $N_f = 2 + 1$ flavors of clover-improved Wilson quarks [47] with clover coefficient set to the tree-level tadpole-improved value and constructed using stout-smeared links [48]. The light-quark masses are tuned to yield a pion mass of $m_\pi \approx 170$ MeV, and the lattice spacing and volume are $a \approx 0.091$ fm [49, 50] and $L^3 \times T = 48^3 \times 96$. The technical details of the lattice QCD calculation are as for the determination of the pion GFFs in Ref. [51] and are summarized below. Additional details, including analysis hyperparameter choices and figures illustrating intermediate results, are included

in the supplementary material.

First, the bare matrix elements of $\hat{T}_g^{\mu\nu}$, and of the singlet and non-singlet quark flavor combinations of the EMT, i.e.,

$$\text{singlet:} \quad \hat{T}_q^{\mu\nu} = \hat{T}_u^{\mu\nu} + \hat{T}_d^{\mu\nu} + \hat{T}_s^{\mu\nu} \tag{3}$$

$$\text{non-singlet:} \quad \hat{T}_{v_1}^{\mu\nu} = \hat{T}_u^{\mu\nu} - \hat{T}_d^{\mu\nu}, \tag{4}$$

$$\hat{T}_{v_2}^{\mu\nu} = \hat{T}_u^{\mu\nu} + \hat{T}_d^{\mu\nu} - 2\hat{T}_s^{\mu\nu}, \tag{5}$$

are constrained from ratios of three-point and two-point functions that are proportional to the bare matrix elements of the EMT, Eq. (1), at large Euclidean times. The three-point function of the gluon EMT is measured on 2511 configurations, averaged over 1024 source positions per configuration, with the gluon EMT measured on gauge fields that have been Wilson flowed [52–54] to $t_{\text{flow}}/a^2 = 2$, for all sink and operator momenta with $|\mathbf{p}'|^2 \leq 10(2\pi/L)^2$ and $|\mathbf{\Delta}|^2 \leq 25(2\pi/L)^2$, and all four spin channels, $s, s' \in \{\pm 1/2\}$. The connected part of the quark three-point function is measured on 1381 configurations using the sequential source method, inverting through the sink for 11 choices of source-sink separation in the range $[6a, 18a]$, with the number of sources varying between 9 and 32 for the different source-sink separations. The momenta measured are $\mathbf{p}' \in 2\pi/L\{(1,0,-1),(-2,-1,0),(-1,-1,-1)\}$ and all $\mathbf{\Delta}$ with $|\mathbf{\Delta}|^2 \leq 25(2\pi/L)^2$, for a single spin channel with $s = s' = 1/2$. The disconnected parts are stochastically estimated on the same 1381 configurations as the connected parts, using 2 samples of Z_4 noise [55], diluting in spacetime using hierarchical probing [56, 57] with 512 Hadamard vectors, and computing the spin-color trace exactly. Measurements are made for all $|\mathbf{p}'|^2 \leq 10(2\pi/L)^2$, $|\mathbf{\Delta}|^2 \leq 25(2\pi/L)^2$, and all four spin channels,

Second, ratios of three- and two-point functions that correspond to the same linear combination of GFFs—as defined in Eq. (1), and up to an overall sign—are averaged. The summation method [58–61] is used to fit the Euclidean time-dependence of the averaged ratios and extract the bare matrix elements. In all cases, 1000 bootstrap ensembles are used to estimate statistical uncertainties, and systematic uncertainties in fits are propagated using model averaging with weights dictated by the Akaike information criterion [62] (AIC) [63–65]. Since connected measurements exist for only a subset of the matrix elements, the disconnected contributions to the bare GFFs of T_q and T_{v_2}[1] are fit separately using all available data, with the results used to obtain better constraints for the subset for which connected parts are available and thus to obtain the full matrix elements of

---

[1] T_{v_1} is purely connected, as the disconnected contributions cancel in the difference.

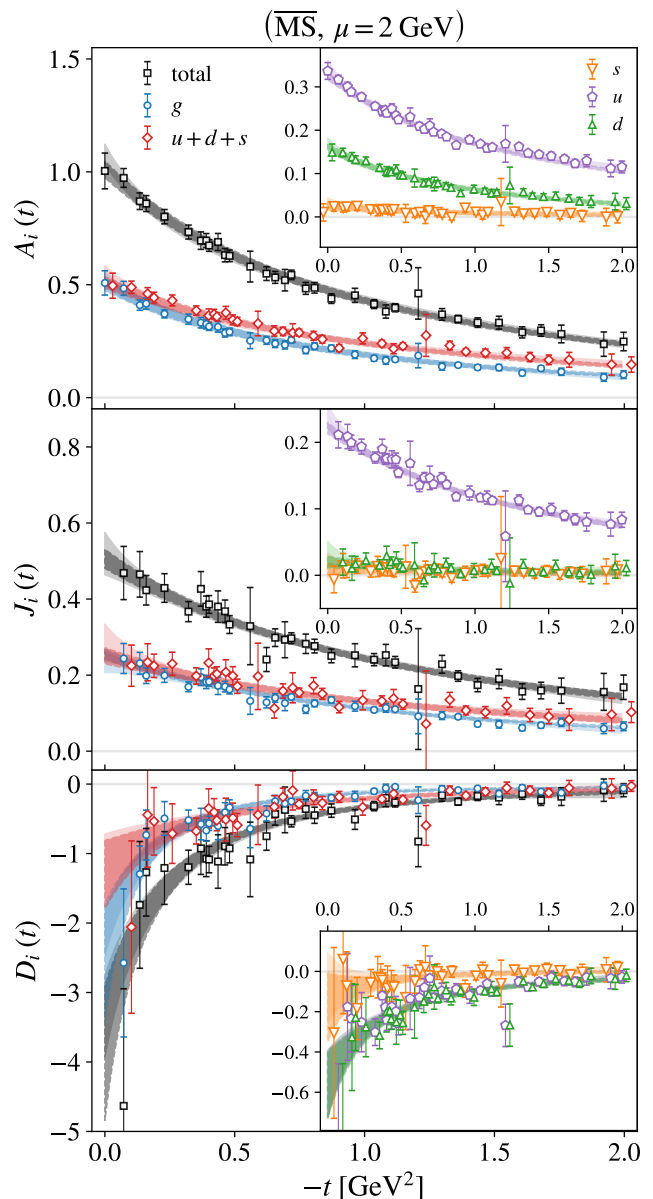

FIG. 1. The three GFFs of the proton, and their decomposition into gluon and total quark contributions, are shown as functions of t. Inset figures show the isosinglet quark GFFs further decomposed into up-, down-, and strange-quark contributions. The total GFFs are renormalization scheme- and scale-independent, while all other GFFs are shown in the $\overline{\text{MS}}$ scheme at $\mu = 2$ GeV. The dark bands represent dipole fits to the data in the case of g and $q = u+d+s$, and linear combinations of the dipole fits to q, v_1, and v_2 in all other cases. The lighter bands show analogous fits using the z-expansion.

T_q and T_{v_2}. Finally, the matrix elements are divided into 34 t-bins using k-means clustering [66], and the GFFs are extracted by solving the resulting linear systems of equations, with the renormalization performed non-perturbatively using the results and procedure presented in Ref. [51].

	Dipole			z-expansion		
	A_i	J_i	D_i	A_i	J_i	D_i
u	0.3255(92)	0.2213(85)	$-0.56(17)$	0.349(11)	0.238(18)	$-0.56(17)$
d	0.1590(92)	0.0197(85)	$-0.57(17)$	0.171(11)	0.033(18)	$-0.56(17)$
s	0.0257(95)	0.0097(82)	$-0.18(17)$	0.032(12)	0.014(19)	$-0.08(17)$
$u+d+s$	0.510(25)	0.251(21)	$-1.30(49)$	0.552(31)	0.286(48)	$-1.20(48)$
g	0.501(27)	0.255(13)	$-2.57(84)$	0.526(31)	0.234(27)	$-2.15(32)$
Total	1.011(37)	0.506(25)	$-3.87(97)$	1.079(44)	0.520(55)	$-3.35(58)$

TABLE I. The flavor decomposition of the momentum fraction, spin, and D-term of the proton, obtained from dipole and z-expansion fits to the proton GFFs, renormalized at $\mu = 2$ GeV in the $\overline{\text{MS}}$ scheme.
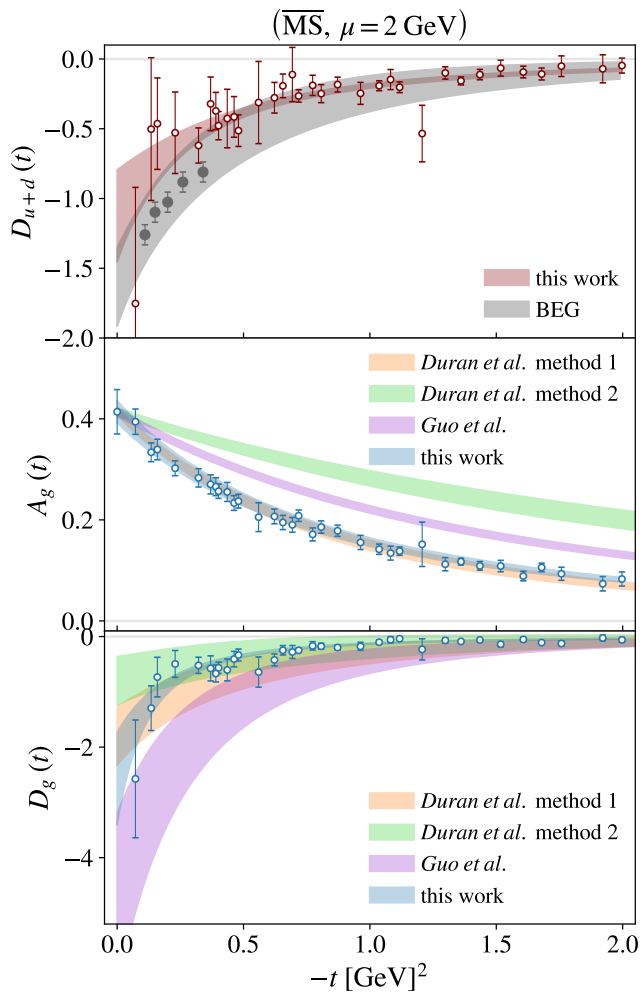

FIG. 2. The proton GFFs $A_g(t)$, $D_g(t)$, and $D_{u+d}(t)$ and corresponding dipole fits from this work are compared with the experimental results of Refs. [24] (BEG), [40] (Duran et al.), and [44] (Guo et al.). For this comparison, the results for $A_g(t)$ are re-scaled such that the gluon momentum fraction is $A_g(0) = 0.414(8)$ [67], which is the value used as an input in the extraction of Refs. [40] and [44]. This does not affect the t-dependence of the GFF.

Results: The flavor decomposition of the renormalized GFFs is presented in Fig. 1. To guide the eye, the GFFs of currents g and q are fit using both a multipole ansatz with $n = 2$ (dipole), chosen as the integer yielding the lowest χ^2 per degree of freedom for the majority of the fits, as well as the more expressive z-expansion [68]. The GFFs are further decomposed to yield the individual quark flavor contributions $\mathbf{G}(t) = (A(t), J(t), D(t))$ from the data and fits for currents q, v_1, and v_2, using

$$\mathbf{G}_u(t) = \frac{1}{3}\mathbf{G}_q(t) + \frac{1}{6}\mathbf{G}_{v_2}(t) + \frac{1}{2}\mathbf{G}_{v_1}(t) , \qquad (6)$$

$$\mathbf{G}_d(t) = \frac{1}{3}\mathbf{G}_q(t) + \frac{1}{6}\mathbf{G}_{v_2}(t) - \frac{1}{2}\mathbf{G}_{v_1}(t) , \qquad (7)$$

$$\mathbf{G}_s(t) = \frac{1}{3}\mathbf{G}_q(t) - \frac{1}{3}\mathbf{G}_{v_2}(t) . \qquad (8)$$

The functional forms of the fit models, along with the resulting fit parameters, are given in the supplementary material.

The flavor decomposition of the forward limits $A(0)$, $J(0)$, and $D(0)$ is summarized in Table I, and can be compared with other recent lattice QCD calculations of the decomposition of the momentum and spin fractions of the proton in Refs. [69, 70]. The sum rules for the total momentum fraction and spin are satisfied, and the total quark and gluon contributions to these quantities are approximately equal. The calculated gluon momentum fraction is, however, several standard deviations larger than the global fit result $A_g(0) = 0.414(8)$ [67], which can likely be attributed to remaining systematic uncertainties that could not be estimated from this calculation using a single ensemble of lattice QCD gauge fields. In particular, the continuum limit has not be taken, and renormalization coefficients were computed on an ensemble with larger lattice spacing and quark masses [51]. The calculated result for the total D-term satisfies the chiral perturbation theory prediction for its upper bound [71], $D(0)/m \leq -1.1(1)$ GeV^{-1}, and is in agreement with chiral models [72–78].

Figure 2 presents a comparison of the dipole fit results with the available experimental results for D_{u+d}, A_g, and
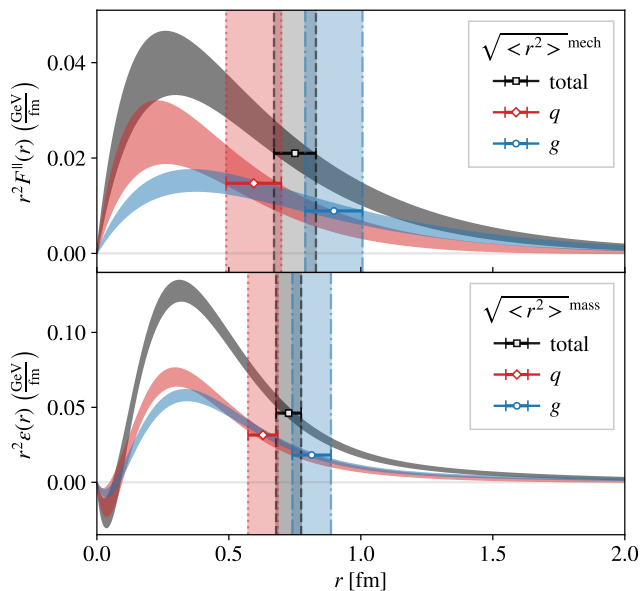
FIG. 3. The quark, gluon, and total contributions to the longitudinal force (upper) and energy (lower) densities in the Breit frame are shown as functions of the radial distance from the center of the proton. The corresponding quark, gluon, and total mechanical and mass radii are marked as data points on the corresponding curves.

D_g, presented in Refs. [24, 40, 44]. The fits to D_{u+d} are found to be consistent, but the uncertainties of the lattice data are comparatively large at the small values of $|t|$ for which experimental data is available. Extractions from new [79] and future experimental data over a larger $|t|$-range, as well as better control of the uncertainties of the lattice QCD result at low $|t|$, will be necessary for a robust comparison. For the gluon GFFs, the lattice QCD results are found to be consistent with the 'holographic QCD' inspired approach [14, 15] (method 1) to the analysis of experimental data in Ref. [40] and disfavor the 'generalized parton distribution' (GPD) inspired approach [80] (method 2). A more recent analysis [44] including an update to the GPD inspired analysis method, as well as additional experimental data [81], is in less tension with the lattice QCD results presented here. These comparisons illustrate the continued synergy and complementarity between lattice and experimental results for these quantities.

Densities: Through the definition in terms of the EMT, and by analogy[2] to mechanical systems, the t-dependence of the GFFs also gives insight into various densities in the proton. Specifically, the Breit-frame dis-

tributions $\varepsilon_i(r)$, $p_i(r)$, and $s_i(r)$, defined as[3]

$$\varepsilon_i(r) = m\left[A_i(t) - \frac{t(D_i(t)+A_i(t)-2J_i(t))}{4m^2}\right]_{\text{FT}}, \quad (9)$$

$$p_i(r) = \frac{1}{6m}\frac{1}{r^2}\frac{d}{dr}r^2\frac{d}{dr}[D_i(t)]_{\text{FT}}, \quad (10)$$

$$s_i(r) = -\frac{1}{4m}r\frac{d}{dr}\frac{1}{r}\frac{d}{dr}[D_i(t)]_{\text{FT}}, \quad (11)$$

where $r = |\mathbf{r}|$,

$$[f(t)]_{\text{FT}} = \int \frac{d^3\mathbf{\Delta}}{(2\pi)^3}e^{-i\mathbf{\Delta}\cdot\mathbf{r}}f(t), \quad (12)$$

and $i \in \{q, g, q+g\}$, can be interpreted as energy, pressure, and shear force distributions respectively [25–27]. The root-mean-square radii of the energy density and the longitudinal force density

$$F_i^{||}(r) = p_i(r) + 2s_i(r)/3 \quad (13)$$

yield the mass and mechanical radii of the proton [27],

$$\langle r_i^2 \rangle^{\text{mass}} = \frac{\int d^3\mathbf{r}\, r^2\varepsilon_i(r)}{\int d^3\mathbf{r}\,\varepsilon_i(r)},$$

$$\langle r_i^2 \rangle^{\text{mech}} = \frac{\int d^3\mathbf{r}\, r^2F_i^{||}(r)}{\int d^3\mathbf{r}\, F_i^{||}(r)}. \quad (14)$$

Figure 3 shows the quark, gluon, and total densities and corresponding radii obtained analytically from the dipole fits to the GFFs. For both densities, the gluonic radius is found to be larger than the quark radius. For the case of the gluon mass radius, the result is consistent with that predicted using the 'holographic QCD' inspired model in the phenomenological extraction of Ref. [40] and the updated analysis of Ref. [44], as shown in Fig. 4. The results for the quark mechanical radius are consistent with a recent extraction from deeply virtual Compton scattering cross sections data [86]. They are also consistent with the soliton model prediction [72, 77] that the proton mechanical radius is slightly smaller than the charge radius [87], and with the equality of the two radii in the non-relativistic limit shown in the bag model [1, 8].

Summary: The flavor decomposition of the proton's $A(t)$, $J(t)$, and $D(t)$ GFFs into their up-, down-, strange-quark, and gluon contributions is determined for the first

---

[2] The physical significance of these analogies is debated [82–85].

---

[3] The quark and gluon contributions to the pressure and energy densities additionally depend on the GFF $\bar{c}_i(t)$, which appears in the decomposition of the matrix elements of $\hat{T}_i^{\mu\nu}$ due to the quark and gluon EMT terms not being individually conserved. This contribution, which is not constrained in this work, vanishes for the total densities since $\bar{c}_q(t) + \bar{c}_g(t)=0$.
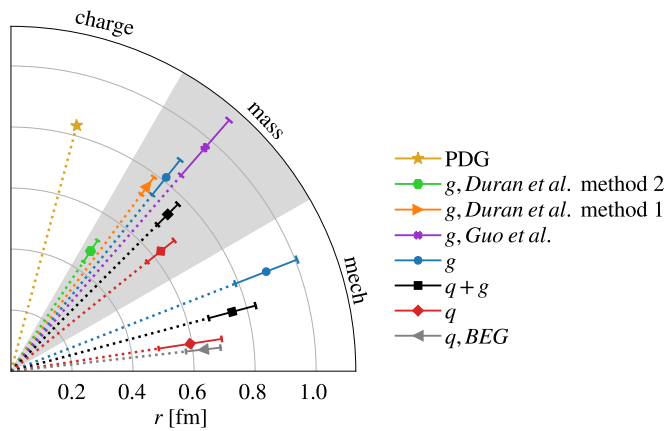
FIG. 4. Comparison of different proton radii. In addition to the results obtained in this work, the charge radius from Ref. [87] (PDG), the gluonic mass radii from Ref. [40] (Duran et al.) and Ref. [44] (Guo et al.), and the quark mechanical radii from Ref. [86] (BEG) are shown. While the latter only includes the light quark contributions, they are compared directly as the strange quark contribution is found to be negligible for this quantity. The uncertainty of the charge radius is too small to be visible.

time for a kinematic range $0 \leq -t \leq 2$ GeV^2, using a first-principles lattice QCD calculation. The results reveal that, while the contributions of quarks and gluons to the proton's momentum, spin, and D-term are approximately equal, the gluon contributions act to extend the radial size of the proton over that defined by the quark contributions as quantified through the mass and mechanical radii encoded in the t-dependence of the GFFs.

The lattice QCD results for the $D_{u+d}(t)$ and $D_g(t)$ GFFs are consistent with the recent experimental results of Refs. [24, 40], but $D_{u+d}(t)$ is constrained over a greater kinematic range. For $A_g(t)$, however, the comparison of first-principles theory with the experimental results of Ref. [40] provides important additional constraints that distinguish between different analyses of the experimental data. Moreover, the results for the separate up-, down-, and strange-quark GFFs presented here are the first constraints on these quantities from first principles theory or from experiment. This work thus sets important benchmarks on these fundamental aspects of proton structure for future measurements at Thomas Jefferson National Accelerator Facility [88–90] and at a future Electron-Ion Collider [91].

[1] M. J. Neubelt, A. Sampino, J. Hudson, K. Tezgin, and P. Schweitzer, Energy momentum tensor and the D-term in the bag model, Phys. Rev. D **101**, 034013 (2020), arXiv:1911.08906 [hep-ph].

[2] M. V. Polyakov and H.-D. Son, Nucleon gravitational form factors from instantons: forces between quark and gluon subsystems, JHEP **09**, 156, arXiv:1808.00155 [hep-ph].

[3] K. Azizi and U. Özdem, Nucleon's energy–momentum tensor form factors in light-cone QCD, Eur. Phys. J. C **80**, 104 (2020), arXiv:1908.06143 [hep-ph].

[4] M. Fujita, Y. Hatta, S. Sugimoto, and T. Ueda, Nucleon D-term in holographic quantum chromodynamics, PTEP **2022**, 093B06 (2022), arXiv:2206.06578 [hep-th].

[5] A. Amor-Quiroz, W. Focillon, C. Lorcé, and S. Rodini, Energy-momentum tensor in the scalar diquark model, (2023), arXiv:2304.10339 [hep-ph].

[6] D. Chakrabarti, C. Mondal, A. Mukherjee, S. Nair, and X. Zhao, Gravitational form factors and mechanical properties of proton in a light-front quark-diquark model, Phys. Rev. D **102**, 113011 (2020), arXiv:2010.04215 [hep-ph].

[7] P. Choudhary, B. Gurjar, D. Chakrabarti, and

A. Mukherjee, Gravitational form factors and mechanical properties of the proton: Connections between distributions in 2D and 3D, Phys. Rev. D **106**, 076004 (2022), arXiv:2206.12206 [hep-ph].

[8] C. Lorcé, P. Schweitzer, and K. Tezgin, 2D energy-momentum tensor distributions of nucleon in a large-Nc quark model from ultrarelativistic to nonrelativistic limit, Phys. Rev. D **106**, 014012 (2022), arXiv:2202.01192 [hep-ph].

[9] S. Owa, A. W. Thomas, and X. G. Wang, Effect of the pion field on the distributions of pressure and shear in the proton, Phys. Lett. B **829**, 137136 (2022), arXiv:2106.00929 [hep-ph].

[10] I. V. Anikin, Gravitational form factors within light-cone sum rules at leading order, Phys. Rev. D **99**, 094026 (2019), arXiv:1902.00094 [hep-ph].

[11] H.-Y. Won, J.-Y. Kim, and H.-C. Kim, Gravitational form factors of the baryon octet with flavor SU(3) symmetry breaking, Phys. Rev. D **106**, 114009 (2022), arXiv:2210.03320 [hep-ph].

[12] R. Fiore, L. Jenkovszky, and M. Oleksiienko, On matter and pressure distribution in nucleons, (2021), arXiv:2112.00605 [hep-ph].

[13] K. A. Mamo and I. Zahed, Diffractive photoproduction of J/ψ and Υ using holographic QCD: gravitational form factors and GPD of gluons in the proton, Phys. Rev. D **101**, 086003 (2020), arXiv:1910.04707 [hep-ph].

[14] K. A. Mamo and I. Zahed, J/ψ near threshold in holographic QCD: A and D gravitational form factors, Phys. Rev. D **106**, 086004 (2022), arXiv:2204.08857 [hep-ph].

[15] K. A. Mamo and I. Zahed, Nucleon mass radii and distribution: Holographic QCD, Lattice QCD and GlueX data, Phys. Rev. D **103**, 094010 (2021), arXiv:2103.03186 [hep-ph].

[16] G. F. de Téramond, H. G. Dosch, T. Liu, R. S. Sufian, S. J. Brodsky, and A. Deur (HLFHS), Gluon matter distribution in the proton and pion from extended holographic light-front QCD, Phys. Rev. D **104**, 114005 (2021), arXiv:2107.01231 [hep-ph].

[17] C. Alexandrou et al., Moments of nucleon generalized parton distributions from lattice QCD simulations at physical pion mass, Phys. Rev. D **101**, 034519 (2020), arXiv:1908.10706 [hep-lat].

[18] P. Shanahan and W. Detmold, Pressure Distribution and Shear Forces inside the Proton, Phys. Rev. Lett. **122**, 072003 (2019), arXiv:1810.07589 [nucl-th].

[19] P. Shanahan and W. Detmold, Gluon gravitational form factors of the nucleon and the pion from lattice QCD, Phys. Rev. D **99**, 014511 (2019), arXiv:1810.04626 [hep-lat].

[20] D. A. Pefkou, D. C. Hackett, and P. E. Shanahan, Gluon gravitational structure of hadrons of different spin, Phys. Rev. D **105**, 054509 (2022), arXiv:2107.10368 [hep-lat].

[21] G. S. Bali, S. Collins, M. Göckeler, R. Rödl, A. Schäfer, and A. Sternbeck, Nucleon generalized form factors from two-flavor lattice QCD, Phys. Rev. D **100**, 014507 (2019), arXiv:1812.08256 [hep-lat].

[22] H.-Y. Won, H.-C. Kim, and J.-Y. Kim, Mechanical structure of the nucleon and the baryon octet, (2023), arXiv:2310.04670 [hep-ph].

[23] Y. Guo, X. Ji, and F. Yuan, Proton's gluon GPDs at large skewness and gravitational form factors from near threshold heavy quarkonium photo-production, (2023),

[24] V. Burkert, L. Elouadrhiri, and F. Girod, The pressure distribution inside the proton, Nature **557**, 396 (2018).

[25] C. Lorcé, H. Moutarde, and A. P. Trawiński, Revisiting the mechanical properties of the nucleon, Eur. Phys. J. C **79**, 89 (2019), arXiv:1810.09837 [hep-ph].

[26] M. Polyakov, Generalized parton distributions and strong forces inside nucleons and nuclei, Phys. Lett. B **555**, 57 (2003), arXiv:hep-ph/0210165.

[27] M. V. Polyakov and P. Schweitzer, Forces inside hadrons: pressure, surface tension, mechanical radius, and all that, Int. J. Mod. Phys. A **33**, 1830025 (2018), arXiv:1805.06596 [hep-ph].

[28] V. D. Burkert, L. Elouadrhiri, F. X. Girod, C. Lorcé, P. Schweitzer, and P. E. Shanahan, Colloquium: Gravitational Form Factors of the Proton, (2023), arXiv:2303.08347 [hep-ph].

[29] N. K. Nielsen, The Energy Momentum Tensor in a Non-abelian Quark Gluon Theory, Nucl. Phys. B **120**, 212 (1977).

[30] F. J. Belinfante, Consequences of the postulate of a complete commuting set of observables in quantum electrodynamics, Phys. Rev. **128**, 2832 (1962).

[31] B. L. G. Bakker, E. Leader, and T. L. Trueman, A Critique of the angular momentum sum rules and a new angular momentum sum rule, Phys. Rev. D **70**, 114001 (2004), arXiv:hep-ph/0406139.

[32] X.-D. Ji, Gauge-Invariant Decomposition of Nucleon Spin, Phys. Rev. Lett. **78**, 610 (1997), arXiv:hep-ph/9603249.

[33] I. Y. Kobzarev and L. B. Okun, GRAVITATIONAL INTERACTION OF FERMIONS, Zh. Eksp. Teor. Fiz. **43**, 1904 (1962).

[34] H. Pagels, Energy-Momentum Structure Form Factors of Particles, Phys. Rev. **144**, 1250 (1966).

[35] M. V. Polyakov and C. Weiss, Skewed and double distributions in pion and nucleon, Phys. Rev. D **60**, 114017 (1999), arXiv:hep-ph/9902451.

[36] Z. Fan, H.-W. Lin, and M. Zeilbeck, Nonperturbatively renormalized nucleon gluon momentum fraction in the continuum limit of Nf=2+1+1 lattice QCD, Phys. Rev. D **107**, 034505 (2023), arXiv:2208.00980 [hep-lat].

[37] J. J. Ethier and E. R. Nocera, Parton Distributions in Nucleons and Nuclei, Ann. Rev. Nucl. Part. Sci. **70**, 43 (2020), arXiv:2001.07722 [hep-ph].

[38] W. Detmold, R. G. Edwards, J. J. Dudek, M. Engelhardt, H.-W. Lin, S. Meinel, K. Orginos, and P. Shanahan (USQCD), Hadrons and Nuclei, Eur. Phys. J. A **55**, 193 (2019), arXiv:1904.09512 [hep-lat].

[39] K.-F. Liu, Status on lattice calculations of the proton spin decomposition, AAPPS Bull. **32**, 8 (2022), arXiv:2112.08416 [hep-lat].

[40] B. Duran et al., Determining the gluonic gravitational form factors of the proton, Nature **615**, 813 (2023), arXiv:2207.05212 [nucl-ex].

[41] P. Hagler et al. (LHPC), Nucleon Generalized Parton Distributions from Full Lattice QCD, Phys. Rev. D **77**, 094502 (2008), arXiv:0705.4295 [hep-lat].

[42] H.-W. Lin, Nucleon Tomography and Generalized Parton Distribution at Physical Pion Mass from Lattice QCD, Phys. Rev. Lett. **127**, 182001 (2021), arXiv:2008.12474 [hep-ph].

[43] C. Alexandrou et al., Moments of the nucleon transverse quark spin densities using lattice QCD, Phys. Rev. D

arXiv:2308.13006 [hep-ph].

107, 054504 (2023), arXiv:2202.09871 [hep-lat].

[44] Y. Guo, X. Ji, Y. Liu, and J. Yang, Updated analysis of near-threshold heavy quarkonium production for probe of proton's gluonic gravitational form factors, Phys. Rev. D **108**, 034003 (2023), arXiv:2305.06992 [hep-ph].

[45] R. Edwards, R. Gupta, N. Joó, K. Orginos, D. Richards, F. Winter, and B. Yoon, U.s. 2+1 flavor clover lattice generation program, unpublished (2016).

[46] M. Lüscher and P. Weisz, On-Shell Improved Lattice Gauge Theories, Commun. Math. Phys. **97**, 59 (1985), [Erratum: Commun.Math.Phys. 98, 433 (1985)].

[47] B. Sheikholeslami and R. Wohlert, Improved Continuum Limit Lattice Action for QCD with Wilson Fermions, Nucl. Phys. B **259**, 572 (1985).

[48] C. Morningstar and M. J. Peardon, Analytic smearing of SU(3) link variables in lattice QCD, Phys. Rev. D **69**, 054501 (2004), arXiv:hep-lat/0311018.

[49] S. Park, R. Gupta, B. Yoon, S. Mondal, T. Bhattacharya, Y.-C. Jang, B. Joó, and F. Winter (Nucleon Matrix Elements (NME)), Precision nucleon charges and form factors using (2+1)-flavor lattice QCD, Phys. Rev. D **105**, 054505 (2022), arXiv:2103.05599 [hep-lat].

[50] S. Borsanyi et al. (BMW), High-precision scale setting in lattice QCD, JHEP **09**, 010, arXiv:1203.4469 [hep-lat].

[51] D. C. Hackett, P. R. Oare, D. A. Pefkou, and P. E. Shanahan, Gravitational form factors of the pion from lattice QCD, (2023), arXiv:2307.11707 [hep-lat].

[52] M. Lüscher, Properties and uses of the Wilson flow in lattice QCD, JHEP **08**, 071, [Erratum: JHEP 03, 092 (2014)], arXiv:1006.4518 [hep-lat].

[53] R. Narayanan and H. Neuberger, Infinite N phase transitions in continuum Wilson loop operators, JHEP **03**, 064, arXiv:hep-th/0601210.

[54] R. Lohmayer and H. Neuberger, Continuous smearing of Wilson Loops., Proc. Sci. **Lattice 2011**, 249 (2012), arXiv:1110.3522 [hep-lat].

[55] M. Hutchinson, A stochastic estimator of the trace of the influence matrix for laplacian smoothing splines, Communications in Statistics - Simulation and Computation **19**, 433 (1990), https://doi.org/10.1080/03610919008812866.

[56] A. Stathopoulos, J. Laeuchli, and K. Orginos, Hierarchical probing for estimating the trace of the matrix inverse on toroidal lattices, SIAM J. Sci. Comput. **35**, S299–S322 (2013), arXiv:1302.4018 [hep-lat].

[57] A. S. Gambhir, *Disconnected Diagrams in Lattice QCD*, Ph.D. thesis, William-Mary Coll. (2017).

[58] S. Capitani, M. Della Morte, G. von Hippel, B. Jäger, A. Juttner, B. Knippschild, H. B. Meyer, and H. Wittig, The nucleon axial charge from lattice QCD with controlled errors, Phys. Rev. D **86**, 074502 (2012), arXiv:1205.0180 [hep-lat].

[59] L. Maiani, G. Martinelli, M. L. Paciello, and B. Taglienti, Scalar Densities and Baryon Mass Differences in Lattice QCD With Wilson Fermions, Nucl. Phys. B **293**, 420 (1987).

[60] S. J. Dong, K. F. Liu, and A. G. Williams, Lattice calculation of the strangeness magnetic moment of the nucleon, Phys. Rev. D **58**, 074504 (1998), arXiv:hep-ph/9712483.

[61] D. Djukanovic, T. Harris, G. von Hippel, P. M. Junnarkar, H. B. Meyer, D. Mohler, K. Ottnad, T. Schulz, J. Wilhelm, and H. Wittig, Isovector electromagnetic form factors of the nucleon from lattice QCD and the proton radius puzzle, Phys. Rev. D **103**, 094522 (2021), arXiv:2102.07460 [hep-lat].

[62] H. Akaike, Information Theory and an Extension of the Maximum Likelihood Principle (Springer Science+Business Media, New York, 1998).

[63] W. I. Jay and E. T. Neil, Bayesian model averaging for analysis of lattice field theory results, Phys. Rev. D **103**, 114502 (2021), arXiv:2008.01069 [stat.ME].

[64] E. Rinaldi, S. Syritsyn, M. L. Wagman, M. I. Buchoff, C. Schroeder, and J. Wasem, Neutron-antineutron oscillations from lattice QCD, Phys. Rev. Lett. **122**, 162001 (2019), arXiv:1809.00246 [hep-lat].

[65] S. R. Beane, E. Chang, W. Detmold, K. Orginos, A. Parreño, M. J. Savage, and B. C. Tiburzi (NPLQCD), Ab initio Calculation of the np→dγ Radiative Capture Process, Phys. Rev. Lett. **115**, 132001 (2015), arXiv:1505.02422 [hep-lat].

[66] D. Steinberg, kmeans1d, https://github.com/dstein64/kmeans1d (2019).

[67] T.-J. Hou et al., New CTEQ global analysis of quantum chromodynamics with high-precision data from the LHC, Phys. Rev. D **103**, 014013 (2021), arXiv:1912.10053 [hep-ph].

[68] R. J. Hill and G. Paz, Model independent extraction of the proton charge radius from electron scattering, Phys. Rev. D **82**, 113005 (2010), arXiv:1008.4619 [hep-ph].

[69] G. Wang, Y.-B. Yang, J. Liang, T. Draper, and K.-F. Liu (χQCD), Proton momentum and angular momentum decompositions with overlap fermions, Phys. Rev. D **106**, 014512 (2022), arXiv:2111.09329 [hep-lat].

[70] C. Alexandrou, S. Bacchio, M. Constantinou, J. Finkenrath, K. Hadjiyiannakou, K. Jansen, G. Koutsou, H. Panagopoulos, and G. Spanoudes, Complete flavor decomposition of the spin and momentum fraction of the proton using lattice QCD simulations at physical pion mass, Phys. Rev. D **101**, 094513 (2020), arXiv:2003.08486 [hep-lat].

[71] J. Gegelia and M. V. Polyakov, A bound on the nucleon Druck-term from chiral EFT in curved space-time and mechanical stability conditions, Phys. Lett. B **820**, 136572 (2021), arXiv:2104.13954 [hep-ph].

[72] K. Goeke, J. Grabis, J. Ossmann, M. V. Polyakov, P. Schweitzer, A. Silva, and D. Urbano, Nucleon form-factors of the energy momentum tensor in the chiral quark-soliton model, Phys. Rev. D **75**, 094021 (2007), arXiv:hep-ph/0702030.

[73] P. Schweitzer, S. Boffi, and M. Radici, Polynomiality of unpolarized off forward distribution functions and the D term in the chiral quark soliton model, Phys. Rev. D **66**, 114004 (2002), arXiv:hep-ph/0207230.

[74] J. Ossmann, M. V. Polyakov, P. Schweitzer, D. Urbano, and K. Goeke, The Generalized parton distribution function (E**u + E**d)(x,xi,t) of the nucleon in the chiral quark soliton model, Phys. Rev. D **71**, 034011 (2005), arXiv:hep-ph/0411172.

[75] K. Goeke, J. Grabis, J. Ossmann, P. Schweitzer, A. Silva, and D. Urbano, The pion mass dependence of the nucleon form-factors of the energy momentum tensor in the chiral quark-soliton model, Phys. Rev. C **75**, 055207 (2007), arXiv:hep-ph/0702031.

[76] M. Wakamatsu, On the D-term of the nucleon generalized parton distributions, Phys. Lett. B **648**, 181 (2007), arXiv:hep-ph/0701057.

[77] C. Cebulla, K. Goeke, J. Ossmann, and P. Schweitzer, The Nucleon form-factors of the energy momentum tensor in the Skyrme model, Nucl. Phys. A **794**, 87 (2007), arXiv:hep-ph/0703025.

[78] J.-H. Jung, U. Yakhshiev, and H.-C. Kim, Energy–momentum tensor form factors of the nucleon within a π–ρ–ω soliton model, J. Phys. G **41**, 055107 (2014), arXiv:1310.8064 [hep-ph].

[79] P. Chatagnon *et al.* (CLAS), First Measurement of Timelike Compton Scattering, Phys. Rev. Lett. **127**, 262501 (2021), arXiv:2108.11746 [hep-ex].

[80] Y. Guo, X. Ji, and Y. Liu, QCD Analysis of Near-Threshold Photon-Proton Production of Heavy Quarkonium, Phys. Rev. D **103**, 096010 (2021), arXiv:2103.11506 [hep-ph].

[81] S. Adhikari *et al.* (GlueX), Measurement of the J/ψ photoproduction cross section over the full near-threshold kinematic region, Phys. Rev. C **108**, 025201 (2023), arXiv:2304.03845 [nucl-ex].

[82] X. Ji and Y. Liu, Momentum-Current Gravitational Multipoles of Hadrons, Phys. Rev. D **106**, 034028 (2022), arXiv:2110.14781 [hep-ph].

[83] R. L. Jaffe, Ambiguities in the definition of local spatial densities in light hadrons, Phys. Rev. D **103**, 016017 (2021), arXiv:2010.15887 [hep-ph].

[84] J. Y. Panteleeva, E. Epelbaum, J. Gegelia, and U. G. Meißner, Definition of gravitational local spatial densities for spin-0 and spin-1/2 systems, Eur. Phys. J. C **83**, 617 (2023), arXiv:2211.09596 [hep-ph].

[85] A. Freese and G. A. Miller, Unified formalism for electromagnetic and gravitational probes: Densities, Phys. Rev. D **105**, 014003 (2022), arXiv:2108.03301 [hep-ph].

[86] V. D. Burkert, L. Elouadrhiri, and F. X. Girod, The mechanical radius of the proton, (2023), arXiv:2310.11568 [hep-ph].

[87] R. L. Workman *et al.* (Particle Data Group), Review of Particle Physics, PTEP **2022**, 083C01 (2022).

[88] J. Arrington *et al.* (Jefferson Lab SoLID), The solenoidal large intensity device (SoLID) for JLab 12 GeV, J. Phys. G **50**, 110501 (2023), arXiv:2209.13357 [nucl-ex].

[89] V. D. Burkert, Jefferson lab at 12 gev: The science program, Annual Review of Nuclear and Particle Science **68**, 405 (2018), https://doi.org/10.1146/annurev-nucl-101917-021129.

[90] J. Arrington *et al.*, Physics with CEBAF at 12 GeV and future opportunities, Prog. Part. Nucl. Phys. **127**, 103985 (2022), arXiv:2112.00060 [nucl-ex].

[91] R. Abdul Khalek *et al.*, Science Requirements and Detector Concepts for the Electron-Ion Collider: EIC Yellow Report, Nucl. Phys. A **1026**, 122447 (2022), arXiv:2103.05419 [physics.ins-det].

[92] R. G. Edwards and B. Joó (SciDAC Collaboration, LHPC Collaboration, UKQCD Collaboration), The Chroma software system for lattice QCD, Nucl.Phys.Proc.Suppl. **140**, 832 (2005), arXiv:hep-lat/0409003 [hep-lat].

[93] A. Pochinsky, Qlua, https://usqcd.lns.mit.edu/qlua.

[94] M. Clark, R. Babich, K. Barros, R. Brower, and C. Rebbi, Solving Lattice QCD systems of equations using mixed precision solvers on GPUs, Comput. Phys. Commun. **181**, 1517 (2010), arXiv:0911.3191 [hep-lat].

[95] R. Babich, M. Clark, B. Joó, G. Shi, R. Brower, and S. Gottlieb, Scaling Lattice QCD beyond 100 GPUs, in SC11 International Conference for High Performance Computing, Networking, Storage and Analysis (2011) arXiv:1109.2935 [hep-lat].

[96] M. A. Clark, B. Joó, A. Strelchenko, M. Cheng, A. Gambhir, and R. Brower, Accelerating Lattice QCD Multigrid on GPUs Using Fine-Grained Parallelization, (2016), arXiv:1612.07873 [hep-lat].

[97] F. T. Winter, M. A. Clark, R. G. Edwards, and B. Joó.

[98] B. Joó, D. D. Kalamkar, T. Kurth, K. Vaidyanathan, and A. Walden, Optimizing wilson-dirac operator and linear solvers for intel® knl, in *High Performance Computing*, edited by M. Taufer, B. Mohr, and J. M. Kunkel (Springer International Publishing, Cham, 2016) pp. 415–427.

[99] A. Gambhir, D. Brantley, J. Chang, B. Hörz, H. Monge-Camacho, P. Vranas, and A. Walker-Loud, lalibe, https://github.com/callat-qcd/lalibe (2018).

[100] C. R. Harris, K. J. Millman, S. J. van der Walt, R. Gommers, P. Virtanen, D. Cournapeau, E. Wieser, J. Taylor, S. Berg, N. J. Smith, R. Kern, M. Picus, S. Hoyer, M. H. van Kerkwijk, M. Brett, A. Haldane, J. F. del Río, M. Wiebe, P. Peterson, P. Gérard-Marchant, K. Sheppard, T. Reddy, W. Weckesser, H. Abbasi, C. Gohlke, and T. E. Oliphant, Array programming with NumPy, Nature **585**, 357 (2020).

[101] P. Virtanen, R. Gommers, T. E. Oliphant, M. Haberland, T. Reddy, D. Cournapeau, E. Burovski, P. Peterson, W. Weckesser, J. Bright, S. J. van der Walt, M. Brett, J. Wilson, K. J. Millman, N. Mayorov, A. R. J. Nelson, E. Jones, R. Kern, E. Larson, C. J. Carey, İ. Polat, Y. Feng, E. W. Moore, J. VanderPlas, D. Laxalde, J. Perktold, R. Cimrman, I. Henriksen, E. A. Quintero, C. R. Harris, A. M. Archibald, A. H. Ribeiro, F. Pedregosa, P. van Mulbregt, and SciPy 1.0 Contributors, SciPy 1.0: Fundamental Algorithms for Scientific Computing in Python, Nature Methods **17**, 261 (2020).

[102] J. Reback, W. McKinney, jbrockmendel, J. V. den Bossche, T. Augspurger, P. Cloud, gfyoung, Sinhrks, A. Klein, M. Roeschke, S. Hawkins, J. Tratner, C. She, W. Ayd, T. Petersen, M. Garcia, J. Schendel, A. Hayden, MomIsBestFriend, V. Jancauskas, P. Battiston, S. Seabold, chris b1, h vetinari, S. Hoyer, W. Overmeire, alimcmaster1, K. Dong, C. Whelan, and M. Mehyar, pandas-dev/pandas: Pandas 1.0.3 (2020).

[103] Wes McKinney, Data Structures for Statistical Computing in Python, in *Proceedings of the 9th Python in Science Conference*, edited by Stéfan van der Walt and Jarrod Millman (2010) pp. 56 – 61.

[104] G. P. Lepage, lsqfit v. 11.7 doi:10.5281/zenodo.4037174 (2020), https://github.com/gplepage/lsqfit.

[105] G. P. Lepage, gvar v. 11.9.1 doi:10.5281/zenodo.4290884 (2020), https://github.com/gplepage/gvar.

[106] J. D. Hunter, Matplotlib: A 2d graphics environment, Computing in Science & Engineering **9**, 90 (2007).

[107] J. E. Mandula, G. Zweig, and J. Govaerts, Representations of the Rotation Reflection Symmetry Group of the Four-dimensional Cubic Lattice, Nucl. Phys. B **228**, 91 (1983).

[108] M. Göckeler, R. Horsley, E.-M. Ilgenfritz, H. Perlt, P. E. Rakow, G. Schierholz, and A. Schiller, Lattice operators for moments of the structure functions and their transformation under the hypercubic group, Phys. Rev. D **54**, 5705 (1996), arXiv:hep-lat/9602029.

FURTHER DETAILS OF LATTICE QCD CALCULATION

The momentum-projected two-point correlation function of the proton for spin channel $s \to s'$ is defined as

$$C_{ss'}^{\text{2pt}}(\mathbf{p}, t_s; \mathbf{x}_0, t_0) = \sum_{\mathbf{x}} e^{-i\mathbf{p}\cdot(\mathbf{x}-\mathbf{x}_0)} \text{tr}\big[\Gamma_{s's}\langle \chi(\mathbf{x}, t_s + t_0)\bar{\chi}(\mathbf{x}_0, t_0)\rangle\big], \tag{15}$$

where the interpolating operator $\chi(x)$ is

$$\chi(x) = \epsilon^{abc}\big[\psi_u^{T,b}(x)C\gamma_5\psi_d^c(x)\big]\psi_u^a(x) , \tag{16}$$

with a, b, c being color indices and C the charge conjugation matrix, and the spin-projection matrices are

$$\Gamma_{s's} = \begin{pmatrix} P_+(1 + \gamma_x\gamma_y) & P_+\gamma_z(\gamma_x + i\gamma_y) \\ P_+\gamma_z(\gamma_x - i\gamma_y) & P_+(1 - \gamma_x\gamma_y) \end{pmatrix}_{s's} , \tag{17}$$

with $P_+ \equiv \frac{1}{2}(1 + \gamma_t)$ being the positive-energy projector. $C_{ss'}^{\text{2pt}}$ is computed on quark sources smeared by gauge-invariant Gaussian smearing up to radius $4.5a$, defined using spatially stout-smeared [48] link fields, for 1024 source positions on each of 2511 configurations. The 1024 sources are arranged in two $4^3 \times 8$ grids offset by $(6, 6, 6, 6)$ lattice units, with an overall random offset for each configuration. The two-point functions are projected to all momenta satisfying $|\mathbf{p}|^2 \leq 10(2\pi/L)^2$. To extract the proton energies, the two-point functions are averaged over all momenta of equivalent magnitude, all sources, and the two diagonal spin channels; the results are fit to the functional form

$$C^{\text{2pt}}(\mathbf{p}, t_s) \sim \sum_{n=0} |Z_{\mathbf{p}}^n|^2 e^{-E_{\mathbf{p}}^n t_s}, \tag{18}$$

where $n = 0$ is the ground state. The momentum-averaged correlator for each distinct $|\mathbf{p}|$ is analyzed independently. The parameters $E_{\mathbf{p}}^0$ are determined by model averaging [63] over the results of fits to models with 2 and 3 states, and various ranges $t_{s,\text{min}} \leq t_s < t_{s,\text{max}}(|\mathbf{p}|)$. All $t_{s,\text{min}} \in [1, 15]$ are used, and $t_{s,\text{max}}(|\mathbf{p}|)$ is taken to be the last point before the noise-to-signal ratio exceeds 5%, ranging between 27 for $\mathbf{p}^2 = 0$ to 21 for $\mathbf{p}^2 = 10$. The energies are parameterized as a tower of positive gaps Δ^n, fitted with a log-space prior $\log \Delta^n \sim \log[0.5(1)]$ for each. Wide, uninformative priors are used for the $Z_{\mathbf{p}}^n$. Uncertainties are propagated by bootstrapping as described in the main text, which is reconciled with model averaging as described in Ref. [20].

Figure 5 shows the effective speed of light c computed from the energies obtained as described above, and the dispersion relation $E_{\mathbf{p}} = \sqrt{m^2 + |c\mathbf{p}|^2}$. The 2% deviation of the results from $c = 1$ is small compared to the uncertainties of the GFFs, and therefore energies obtained from the dispersion relation using the fit to the nucleon mass $am = 0.4169$ are used for the remainder of the analysis.
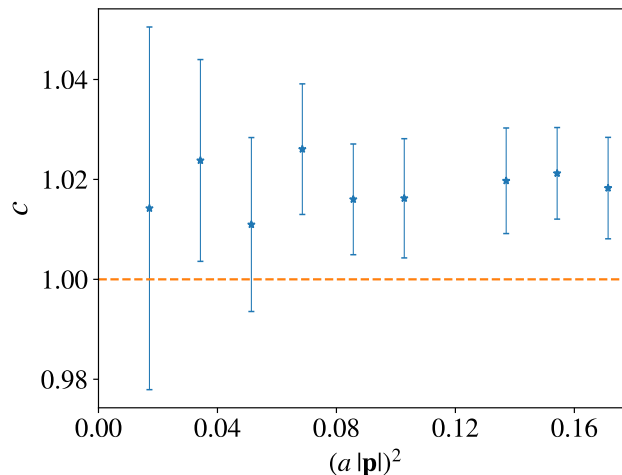

FIG. 5.   The values of c obtained from the dispersion relation $E_{\mathbf{p}} = \sqrt{m^2 + |c\mathbf{p}|^2}$ using the ground state energies extracted from fits to nucleon two-point correlation functions.

t_s	6	7	8	9	10	11	12	13	14	16	18
N_s	9	16	16	16	16	16	16	16	32	32	32

TABLE II. Number of sources N_s for which the connected quark contributions to the three-point function, Eq. (30), are computed for each sink time t_s.

The quark and gluon symmetric EMT contributions in Euclidean space can be defined as

$$\hat{T}_{f,\mu\nu}(x) = \bar{\psi}_f(x)\overleftrightarrow{D}_{\{\mu}\gamma_{\nu\}}\psi_f(x), \tag{19}$$

$$\hat{T}_{g,\mu\nu}(x) = 2\,\mathrm{Tr}\left[F_{\mu\rho}(x)F_{\nu\rho}(x) - \frac{1}{4}\delta_{\mu\nu}F_{\alpha\beta}(x)F_{\alpha\beta}(x)\right], \tag{20}$$

where, up to discretization effects, the Euclidean gluon field strength tensor can be expressed as

$$F_{\mu\nu}(x) = \frac{i}{8g_0}(Q_{\mu\nu}(x) - Q_{\mu\nu}^\dagger(x)), \tag{21}$$

with $Q_{\mu\nu}$ defined in terms of the link fields as

$$\begin{aligned}Q_{\mu\nu}(x) =& U_\mu(x)U_\nu(x+\hat{\mu})U_\mu^\dagger(x+\hat{\nu})U_\nu^\dagger(x) + U_\nu(x)U_\mu^\dagger(x-\hat{\mu}-\hat{\nu})U_\nu^\dagger(x-\hat{\mu})U_\mu(x-\hat{\mu}) \\ &+ U_\mu^\dagger(x-\hat{\mu})U_\nu^\dagger(x-\hat{\mu}-\hat{\nu})U_\mu(x-\hat{\mu}-\hat{\nu})U_\nu(x-\hat{\nu}) + U_\nu^\dagger(x-\hat{\nu})U_\mu(x-\hat{\nu})U_\nu(x-\hat{\mu}-\hat{\nu})U_\mu^\dagger,\end{aligned} \tag{22}$$

and where g_0 is the bare coupling for a tadpole-improved Luscher-Weisz gauge action with tadpole parameter u_0,

$$g_0 = \sqrt{\frac{2N_c}{\beta(1 - \frac{2}{5u_0^2})}}. \tag{23}$$

The symmetric covariant derivative can be expressed as

$$\overleftrightarrow{D}_\mu = \frac{1}{2}\left(\overrightarrow{D}_\mu - \overleftarrow{D}_\mu\right), \tag{24}$$

where

$$\overrightarrow{D}_\mu^E\psi(x) = \frac{1}{2}\left(U_\mu(x)\psi(x+\hat{\mu}) - U_\mu^\dagger(x-\hat{\mu})\psi(x-\hat{\mu})\right) \tag{25}$$

$$\bar{\psi}(x)\overleftarrow{D}_\mu^E = \frac{1}{2}\left(\bar{\psi}(x+\hat{\mu})U_\mu^\dagger(x) - \bar{\psi}(x-\hat{\mu})U_\mu(x-\hat{\mu})\right). \tag{26}$$

On an isotropic hypercubic lattice, the traceless diagonal and off-diagonal components of the EMT transform under two different irreducible representations (irreps) of the hypercubic group, $\tau_1^{(3)}$ and $\tau_3^{(6)}$ [107, 108]. The choice of basis for each irrep that is used in this work is

$$\hat{T}_{\tau_{1,1}^{(3)}} = \frac{1}{2}(\hat{T}_{11} + \hat{T}_{22} - \hat{T}_{33} - \hat{T}_{44}),\ \hat{T}_{\tau_{1,2}^{(3)}} = \frac{1}{\sqrt{2}}(\hat{T}_{11} - \hat{T}_{22}),\ \hat{T}_{\tau_{1,3}^{(3)}} = \frac{1}{\sqrt{2}}(\hat{T}_{33} - \hat{T}_{44}), \tag{27}$$

$$\begin{aligned}\hat{T}_{\tau_{3,1}^{(6)}} &= \frac{1}{\sqrt{2}}(\hat{T}_{12} + \hat{T}_{21}),\ \hat{T}_{\tau_{3,2}^{(6)}} = \frac{1}{\sqrt{2}}(\hat{T}_{13} + \hat{T}_{31})\ ,\hat{T}_{\tau_{3,3}^{(6)}} = \frac{1}{\sqrt{2}}(\hat{T}_{14} + \hat{T}_{41}), \\ \hat{T}_{\tau_{3,4}^{(6)}} &= \frac{1}{\sqrt{2}}(\hat{T}_{23} + \hat{T}_{32}),\ \hat{T}_{\tau_{3,5}^{(6)}} = \frac{1}{\sqrt{2}}(\hat{T}_{24} + \hat{T}_{42}),\ \hat{T}_{\tau_{3,6}^{(6)}} = \frac{1}{\sqrt{2}}(\hat{T}_{34} + \hat{T}_{43}),\end{aligned} \tag{28}$$

which can be transformed to Minkowski space via

$$\text{Euclidean} \to \text{Minkowski}: \hat{T}_{44} \to \hat{T}_{00},\ \hat{T}_{4j} \to -i\hat{T}_{0j},\ \hat{T}_{jk} \to -\hat{T}_{jk}. \tag{29}$$

The three-point functions needed to extract the matrix elements of operator $\hat{T}_{i\mathcal{R}\ell}$, where $\mathcal{R} \in \{\tau_1^{(3)}, \tau_3^{(6)}\}$, ℓ denotes the vector in the basis of the irreps defined in Eqs. (27) and (28), and $i \in \{q, g, v_1, v_2\}$, are defined as

$$C_{i\mathcal{R}\ell ss'}^{\mathrm{3pt}}(\mathbf{p}', t_s; \boldsymbol{\Delta}, \tau; \mathbf{x_0}, t_0) = \sum_{\mathbf{x},\mathbf{y}} e^{-i\mathbf{p}'\cdot(\mathbf{x}-\mathbf{x_0})} e^{i\boldsymbol{\Delta}\cdot(\mathbf{y}-\mathbf{x_0})} \mathrm{tr}\left[\langle\Gamma_{s's}\chi(\mathbf{x}, t_s + t_0)\hat{T}_{i\mathcal{R}\ell}\bar{\chi}(\mathbf{x_0}, t_0)\rangle\right]. \tag{30}$$

In the limit where $(t_s - t_0) \to \infty$ and $(t_s - \tau) \to \infty$, the three-point functions approach the desired matrix elements as:

$$C^{\text{3pt}}_{i\mathcal{R}\ell ss'}(\mathbf{p}', t_s; \mathbf{\Delta}, \tau; \mathbf{x_0}, t_0) \xrightarrow[\substack{(t_s-t_0)\to\infty}]{(t_s-\tau)\to\infty} Z^*_{\mathbf{p}} Z_{\mathbf{p}'} \frac{e^{-E_{\mathbf{p}'}(t_s-t_0)} e^{-(E_{\mathbf{p}}-E_{\mathbf{p}'})(\tau-t_0)}}{4E_{\mathbf{p}'}E_{\mathbf{p}}} \langle N(\mathbf{p}', s') | \hat{T}_{i\mathcal{R}\ell} | N(\mathbf{p}, s) \rangle, \qquad (31)$$

where $\mathbf{p} = \mathbf{p}' - \mathbf{\Delta}$. Three-point functions for the disconnected quark and gluon contributions are constructed by correlating the operator measurements with the grid of 1024 two-point functions described above. The connected quark contributions are measured for a subset of source-sink separations, with different numbers of sources for each as tabulated in Table II. These measurements are averaged over all source positions and 1000 bootstrap ensembles are formed. At the bootstrap level, the following ratios of three- and two-point functions are constructed:

$$
\begin{aligned}
R_{i\mathcal{R}\ell ss'}(\mathbf{p}', t_s; \mathbf{\Delta}, \tau) &= \frac{C^{\text{3pt}}_{i\mathcal{R}\ell ss'}(\mathbf{p}', t_s; \mathbf{\Delta}, \tau)}{C^{\text{2pt}}_{s's'}(\mathbf{p}', t_s)} \sqrt{\frac{C^{\text{2pt}}_{ss}(\mathbf{p}, t_s - \tau) C^{\text{2pt}}_{s's'}(\mathbf{p}', t_s) C^{\text{2pt}}_{s's'}(\mathbf{p}', \tau)}{C^{\text{2pt}}_{s's'}(\mathbf{p}', t_s - \tau) C^{\text{2pt}}_{ss}(\mathbf{p}, t_s) C^{\text{2pt}}_{ss}(\mathbf{p}, \tau)}} \\
&\xrightarrow[t_s\to\infty]{(t_s-\tau)\to\infty} \frac{\text{tr}\left[\Gamma_{s's}(\not{p}' + m) \langle N(\mathbf{p}', s')| \hat{T}_{i\mathcal{R}\ell} |N(\mathbf{p}, s)\rangle (\not{p} + m)\right]}{4\sqrt{E_{\mathbf{p}}E_{\mathbf{p}'}(E_{\mathbf{p}} + m)(E_{\mathbf{p}'} + m)}}.
\end{aligned}
\qquad (32)
$$

The above expression is a linear combination of the GFFs, with known kinematical coefficients. Within each irrep, all ratios for choices $(\ell, \mathbf{p}', \mathbf{\Delta}, s, s')$ that yield identical coefficients up to an overall minus sign are averaged, yielding averaged ratios $\bar{R}_{i\mathcal{R}c}(t; t_s, \tau)$, where c denotes the unique set of coefficients and t the squared momentum transfer associated with it. The averaged ratios yield the matrix elements of interest as

$$\bar{R}_{i\mathcal{R}c}(t; t_s, \tau) \xrightarrow[t_s\to\infty]{(t_s-\tau)\to\infty} \text{ME}_{i\mathcal{R}c}(t), \qquad (33)$$

where $\text{ME}_{i\mathcal{R}c}(t)$ is the rescaled matrix element to be extracted by fitting the Euclidean time dependence of the ratios. This is done using the summation method, wherein one sums over the operator insertion time τ to form summed ratios [58–60]

$$\bar{\Sigma}_{i\mathcal{R}c}(t; t_s, \tau_{\text{cut}}) = \sum_{\tau=\tau_{\text{cut}}}^{t_s - \tau_{\text{cut}}} \bar{R}_{i\mathcal{R}c}(t; t_s, \tau) \xrightarrow[t_s\to\infty]{(t_s-\tau)\to\infty} (t_s - \tau_{\text{cut}} + 1)\text{ME}_{i\mathcal{R}c}(t) + \Lambda_{i\mathcal{R}c}(t; \tau_{\text{cut}}), \qquad (34)$$

where $\Lambda_{i\mathcal{R}c}(t; \tau_{\text{cut}})$ is a t_s-independent constant. $\text{ME}_{i\mathcal{R}c}(t)$ is then extracted by fitting the slope of $\bar{\Sigma}_{i\mathcal{R}c}(t; t_s, \tau_{\text{cut}})$ with respect to t_s.

For the connected data, summed ratios are constructed and fit for all $\tau_{\text{cut}} \in [2, 6]$. Linear summation fits are performed for all ranges $t_{s,\min} < t_s \leq 18$, where $t_{s,\min} \in [6, 14]$ and $t_s = 18$ is the largest available in the dataset. The resulting pool of fits are model-averaged to obtain the final estimate of the matrix element. For the disconnected data, summation fits are performed for $\tau_{\text{cut}} \geq 2$ to all t_s-ranges extending over 5 or more timeslices in the window $[t_{s,\min}, t_{s,\max}]$, where $t_{s,\min} = 6$ for $\tau_1^{(3)}$ and $t_{s,\min} = 10$ for $\tau_3^{(6)}$, which yield the highest p-values for most of the t-bins in the bare GFF fits of both singlet and non-singlet disconnected quark contributions. The maximum sink time is set to $t_{s,\max} = 20$, after which the c-bin ratios become consistent with non-Gaussian noise. For the gluon contribution, in order to avoid the effect of contact terms due to the gradient flow, cuts are made such that $\tau_{\text{cut}} \geq 4$ and $t_{\min} \geq 9$ for the summation fits, while the rest of the fitting details are the same as for the disconnected quark data. Examples of averaged ratios and corresponding summation method fits for all different contributions are shown in Figs. 6 and 7.

The matrix elements of the singlet $u + d + s$ and non-singlet $u + d - 2s$ currents contain both a connected and a disconnected contribution. However, data for the connected contribution are only available for a subset of the kinematics compared to the disconnected contribution, as three-point functions were computed for only three sink momenta and one spin orientation via the sequential source method, inverting through the sink. Discarding a considerable fraction of the disconnected contribution measurements is undesirable, since constraining it is already challenging due to poor signal-to-noise. Instead, the bare disconnected singlet and non-singlet contributions to the GFFs are first fit, by separating the complete set of rescaled matrix elements obtained by the summation fits into 34 momentum t-bins (the same t-bins used for the renormalized GFFs presented in the main text), and inverting the system of equations

$$\mathbf{K}^A_{\mathcal{R}t} A^{\text{bare}}_{i\mathcal{R}t} + \mathbf{K}^J_{\mathcal{R}t} J^{\text{bare}}_{i\mathcal{R}t} + \mathbf{K}^D_{\mathcal{R}t} D^{\text{bare}}_{i\mathcal{R}t} = \mathbf{ME}_{i\mathcal{R}t} \qquad (35)$$

for each t-bin. Here, bold symbols are vectors in the space of c-bins, $\mathbf{K}$ are the kinematic coefficients multiplying the GFFs in the expansion of the rescaled matrix element, as defined by Eqs. (32) and (1), and $i \in \{q^{\text{disco}}, v_2^{\text{disco}}\}$. The

resulting bare GFFs are shown in Fig. 8. These are then used to obtain predictions for the disconnected contributions to the smaller subset of matrix elements for which the connected measurements are available.

In order to investigate how well the summation fits describe the data cumulatively, "effective matrix elements" are defined as functions of t_s by

$$\mathrm{ME}^{\mathrm{eff}}_{i\mathcal{R}c}(t;t_s) = \partial_{t_s}\bar{\Sigma}_{i\mathcal{R}c}(t;t_s) \approx \frac{1}{\delta t_s}\left[\bar{\Sigma}_{i\mathcal{R}c}(t;t_s+\delta t_s) - \bar{\Sigma}_{i\mathcal{R}c}(t;t_s)\right] ,\tag{36}$$

with $\delta t_s = 1$ for all the gluon and quark disconnected data, and for the majority of the quark connected data[4]. The τ_{cut} dependence of the summed ratios is fixed to the minimum value used for the specific contribution, as described above, and is not explicitly shown. The effective matrix elements, which are formed directly from the data, are grouped into the same t-bins used for extraction of the GFFs. One can then obtain "effective" bare GFFs $A^{\mathrm{eff}}_{i\mathcal{R}t}(t_s)$, $J^{\mathrm{eff}}_{i\mathcal{R}t}(t_s)$, and $D^{\mathrm{eff}}_{i\mathcal{R}t}(t_s)$ for each flavor i, irrep $\mathcal{R}$, momentum bin t, and sink time t_s by fitting the overconstrained system of linear equations,

$$\mathbf{K}^A_{\mathcal{R}t}A^{\mathrm{eff}}_{i\mathcal{R}t}(t_s) + \mathbf{K}^J_{\mathcal{R}t}J^{\mathrm{eff}}_{i\mathcal{R}t}(t_s) + \mathbf{K}^D_{\mathcal{R}t}D^{\mathrm{eff}}_{i\mathcal{R}t}(t_s) = \mathbf{ME}^{\mathrm{eff}}_{i\mathcal{R}t}(t_s) ,\tag{37}$$

where $\mathbf{K}^A_{\mathcal{R}t}$, $\mathbf{K}^J_{\mathcal{R}t}$ and $\mathbf{K}^D_{\mathcal{R}t}$ are as in Eq. (35). Figs. 9, 10, and 11 show examples of the bare effective GFFs for all the different contributions and several different t-bins.

GFF MODEL FIT PARAMETERS

The renormalized GFFs presented in Fig. 1 include fits using the n-pole model

$$\mathrm{F}_n(t) = \frac{\alpha}{(1-t/\Lambda^2)^n},\tag{38}$$

with α and Λ being free parameters. All choices $1 \leq n \leq 4$ yield consistent results. The dipole model, $n = 2$, was chosen for the results presented in the main text based on the χ^2/d.o.f. Results are also presented using the z-expansion [68]

$$\mathrm{F}_z(t) = \sum_{k=0}^{k_{\mathrm{max}}} \alpha_k[z(t)]^k,\tag{39}$$

where α_k are free parameters, and

$$z(t) = \frac{\sqrt{t_{\mathrm{cut}}-t}-\sqrt{t_{\mathrm{cut}}-t_0}}{\sqrt{t_{\mathrm{cut}}-t}+\sqrt{t_{\mathrm{cut}}-t_0}},\tag{40}$$

where

$$t_0 = t_{\mathrm{cut}}\left(1 - \sqrt{1+(2\ \mathrm{GeV})^2/t_{\mathrm{cut}}}\right),\tag{41}$$

and $t_{\mathrm{cut}} = 4m_\pi^2$. Fits were performed with k_{max} varied between 2 and 4, and the smallest χ^2/d.o.f is obtained in fits with $k_{\mathrm{max}} = 2$, which is used for the results in the main text. Table III presents the resulting parameters of the dipole and z-expansion fits to $A(t)$, $J(t)$, and $D(t)$, which are used to produce the bands in Fig. 1, along with the corresponding χ^2 per degree of freedom of each fit.

SINGLE-IRREP RENORMALIZED GFFS

The results presented in the main text are the result of a simultaneous fit to both irreps using the procedure and renormalization coefficients of Ref. [51]. The renormalized results for the two irreps must agree in the continuum limit, but can have different discretization artifacts. Since a continuum extrapolation is not performed, Fig. 12 presents the renormalized GFFs obtained by fitting the two irreps separately. Although some tension is observed between the two irreps for some of the GFFs, particularly for $J_g(t)$, the p-values of the combined-irrep fits are comparable to those for the single-irrep fits. In future work, it will be important to repeat this calculation at different lattice spacings in order to better quantify the discretization artifacts.

---

[4] δt_s is set to 2 for the larger sink times of the connected data, since $t_s = 15$ and $t_s = 17$ were not computed.
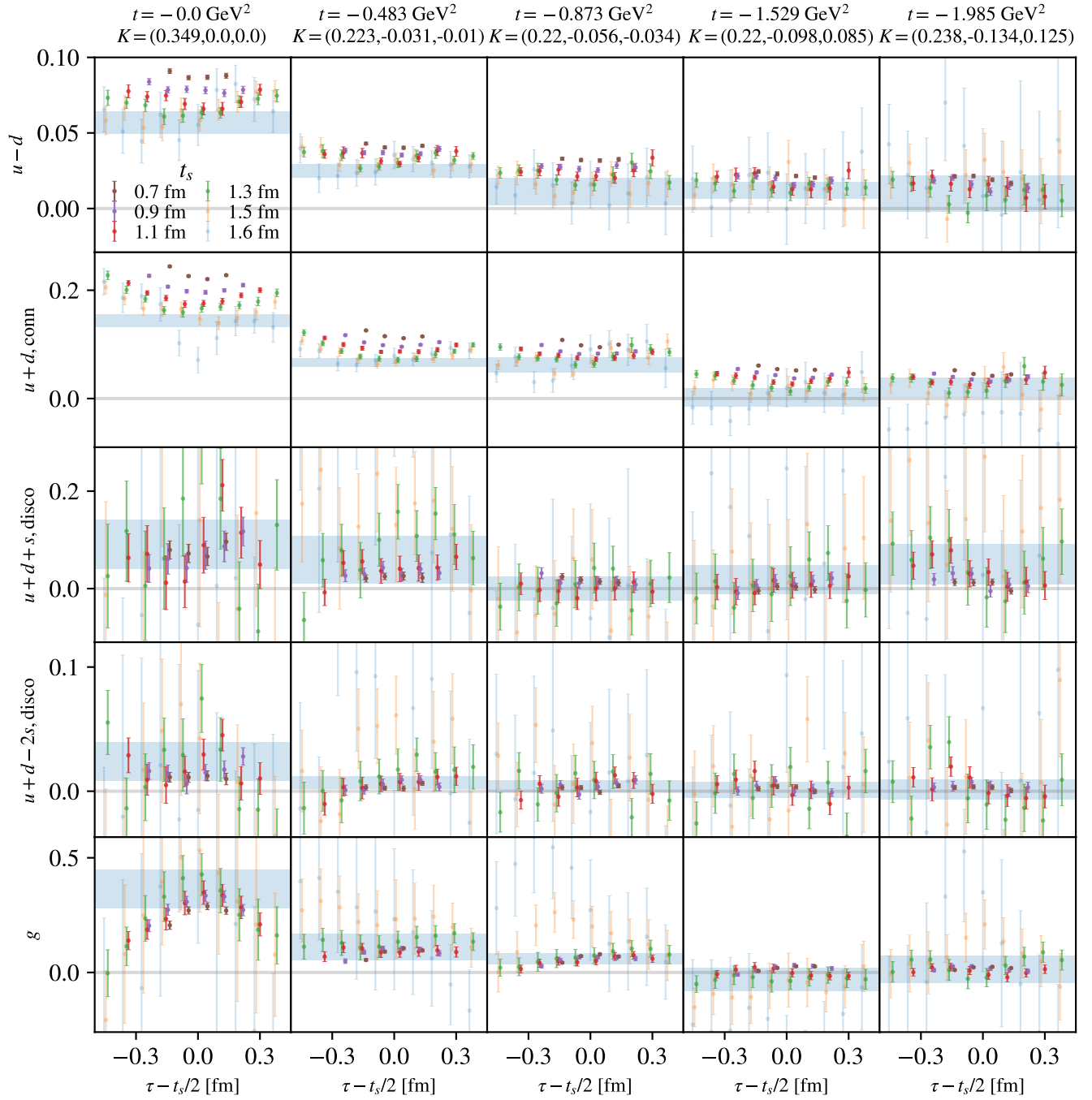
FIG. 6. Examples of averaged ratios, defined following Eq. (32), for $\tau_1^{(3)}$. Each column represents a single ratio, with the corresponding t value and (K^A, K^J, K^D) coefficients shown as column titles. The rows represent the bare $u-d$, the connected part of $u+d$, the disconnected part of $u+d+s$, the disconnected part of $u+d-2s$, and the gluon contributions to the ratio. The overlaid bands show fits to the corresponding ratios obtained via the summation method as described in the text.
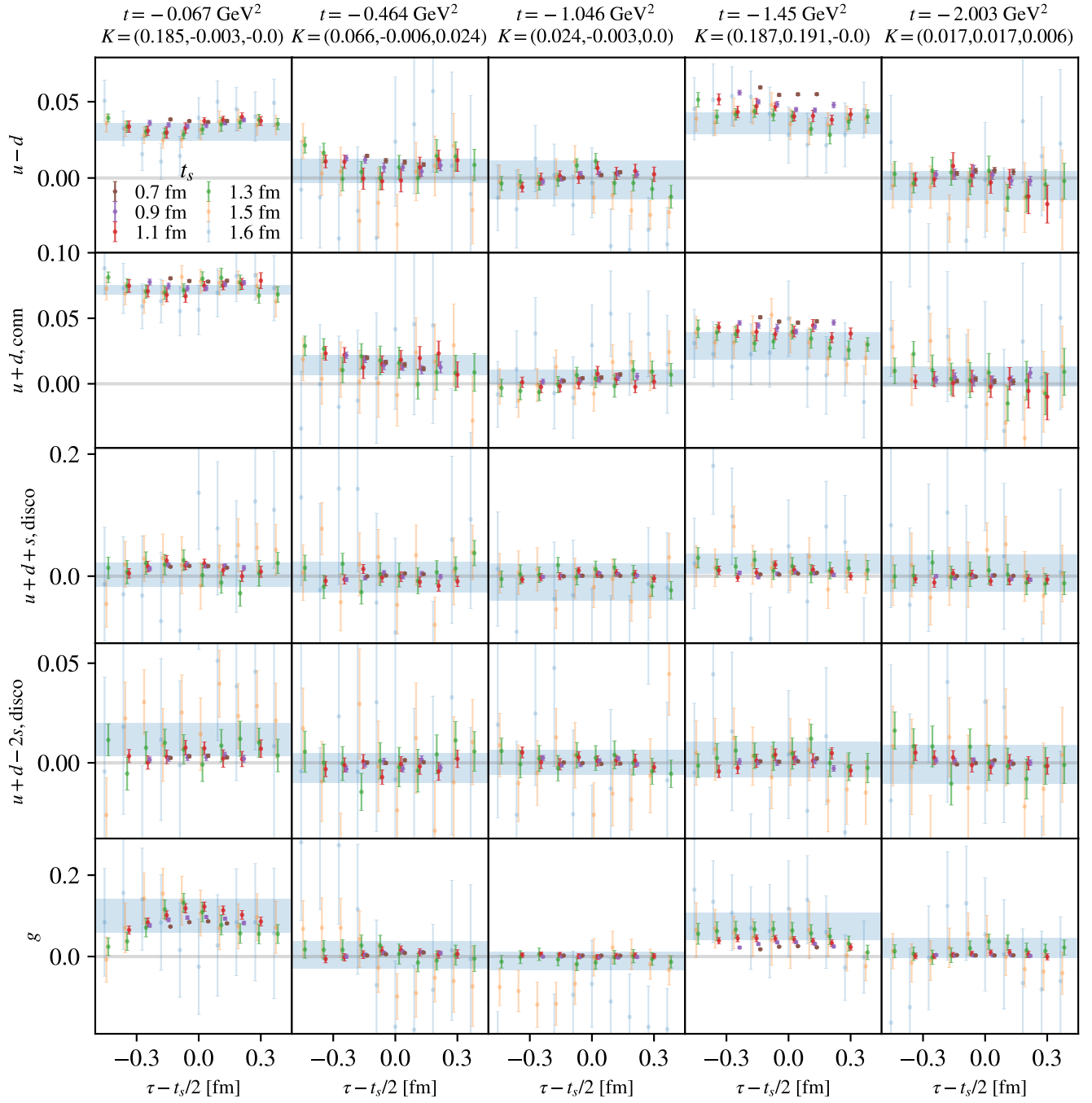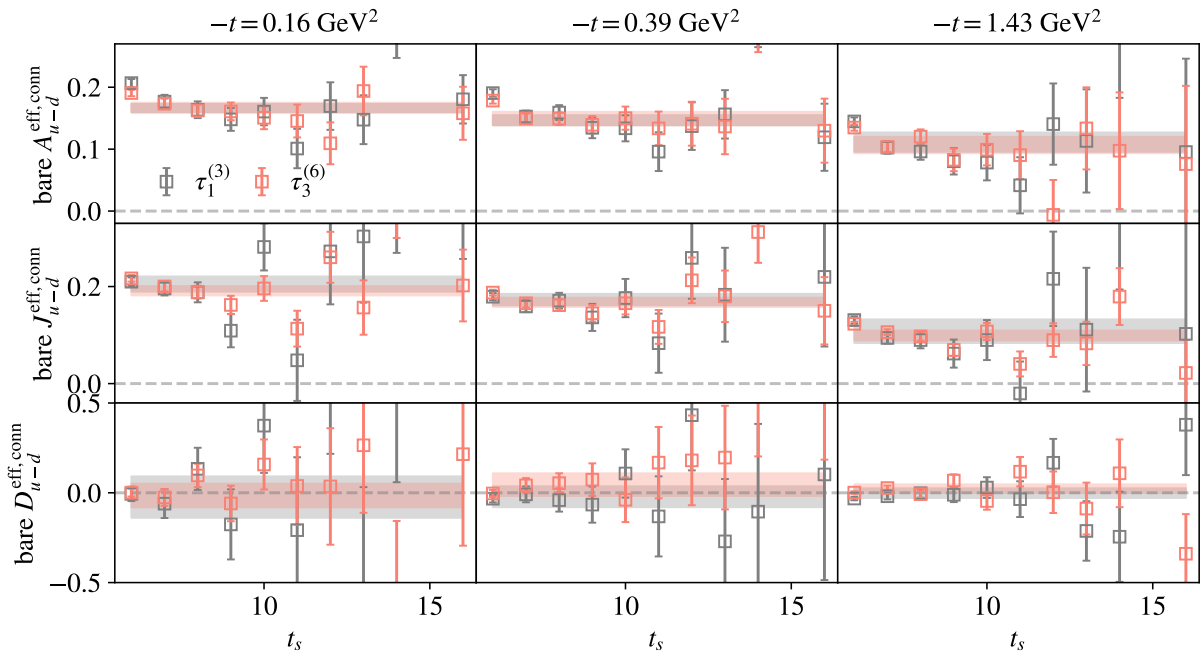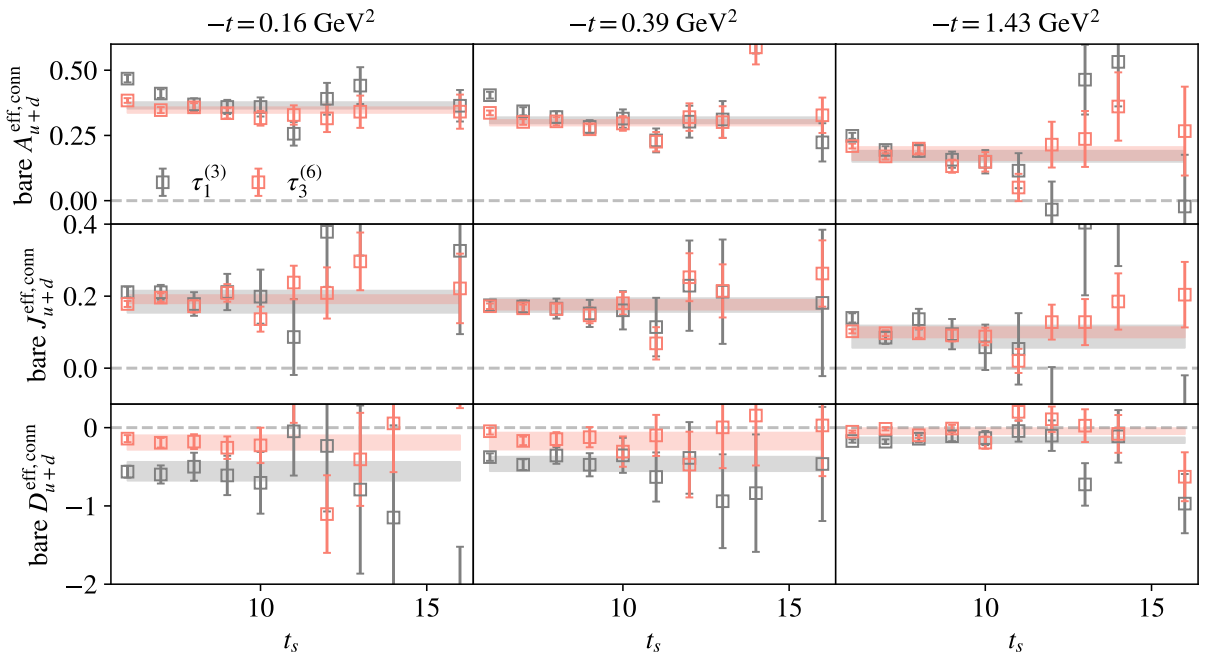
FIG. 7. As in Fig. 6, but for irrep $\tau_3^{(6)}$.
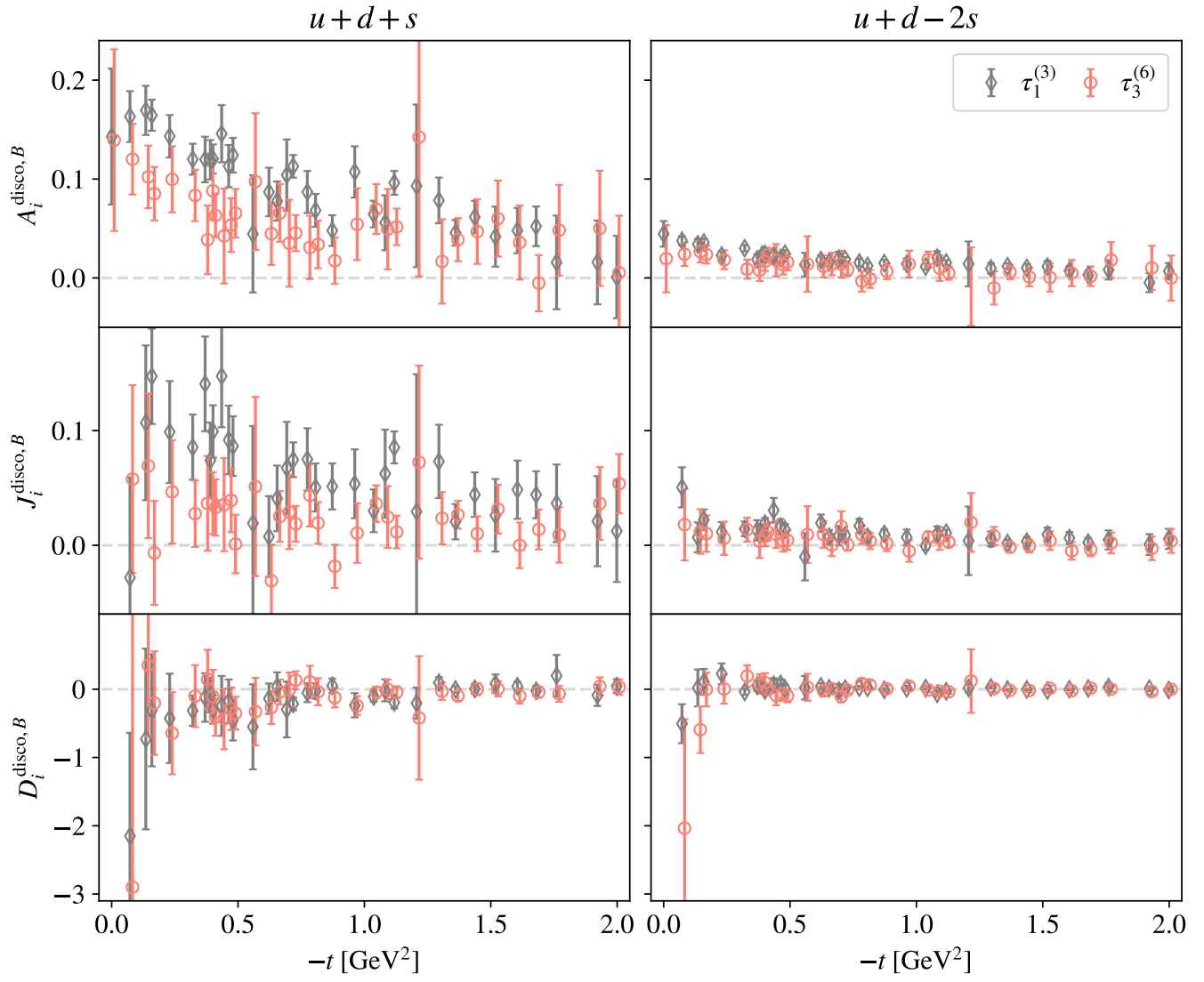
FIG. 8. Bare disconnected quark GFFs for each of the two irreps studied.

FIG. 9. Examples of effective GFFs for three different t-bins of (a) the purely connected $u - d$ and (b) the connected part of the $u + d$ contribution, computed from Eq. (37) using summed ratios with $\tau_{\mathrm{cut}} = 2$. The bands are not fits to the data shown but correspond to bare GFFs obtained by fitting the bare matrix elements used to compute the results from the main text.

9
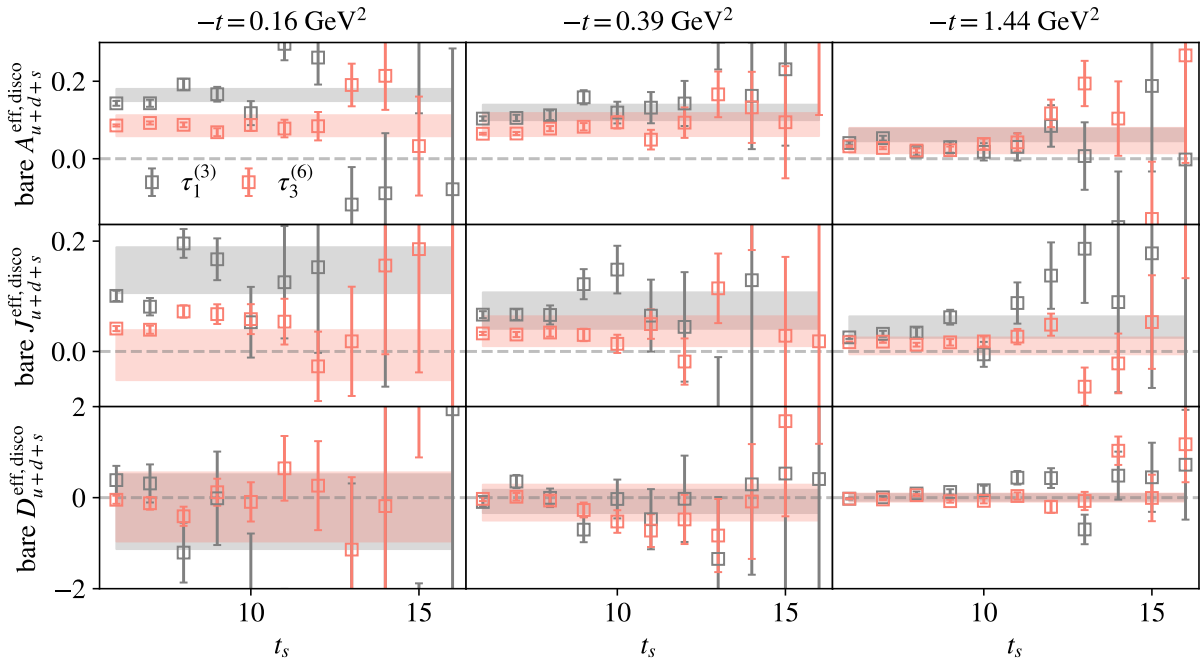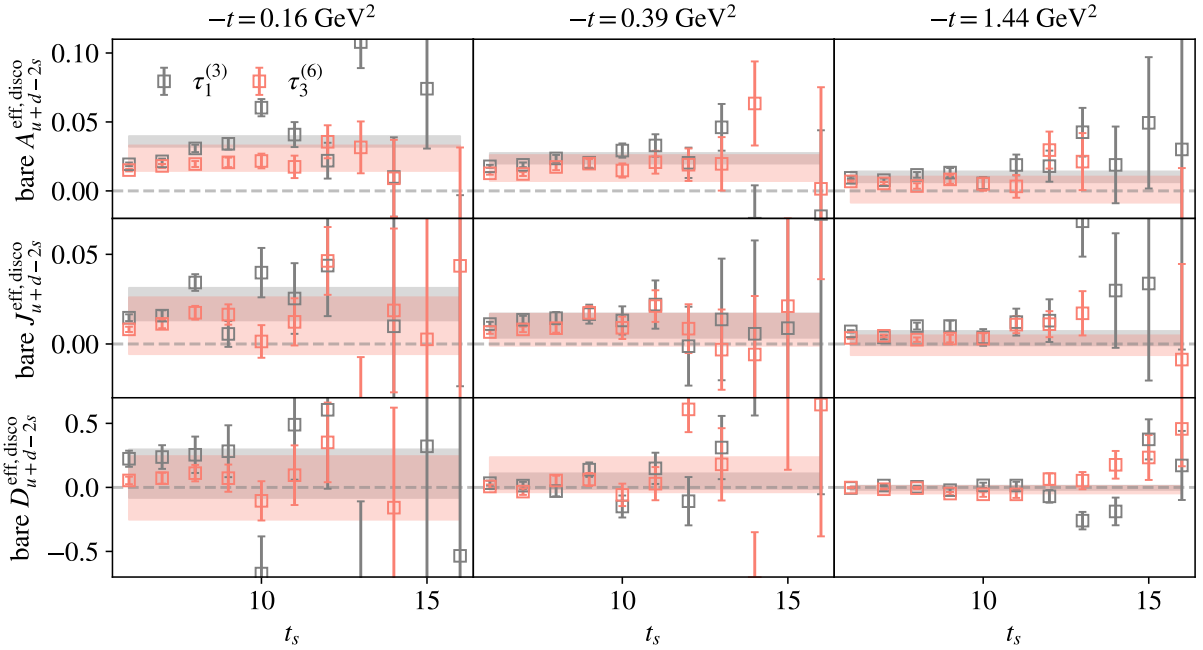
FIG. 10. Examples of effective GFFs for three different t-bins of the disconnected part of the (a) $u + d + s$ and (b) $u + d - 2s$ contribution, computed from Eq. (37) using summed ratios with $\tau_{\mathrm{cut}} = 2$. The bands are not fits to the data shown but correspond to bare GFFs obtained by fitting the bare matrix elements used to compute the results from the main text.

FIG. 11. Examples of effective GFFs for three different t-bins of the gluon contribution, computed from Eq. (37) using summed ratios with $\tau_{\text{cut}} = 4$. The bands are not fits to the data shown but correspond to bare GFFs obtained by fitting the bare matrix elements used to compute the results from the main text.
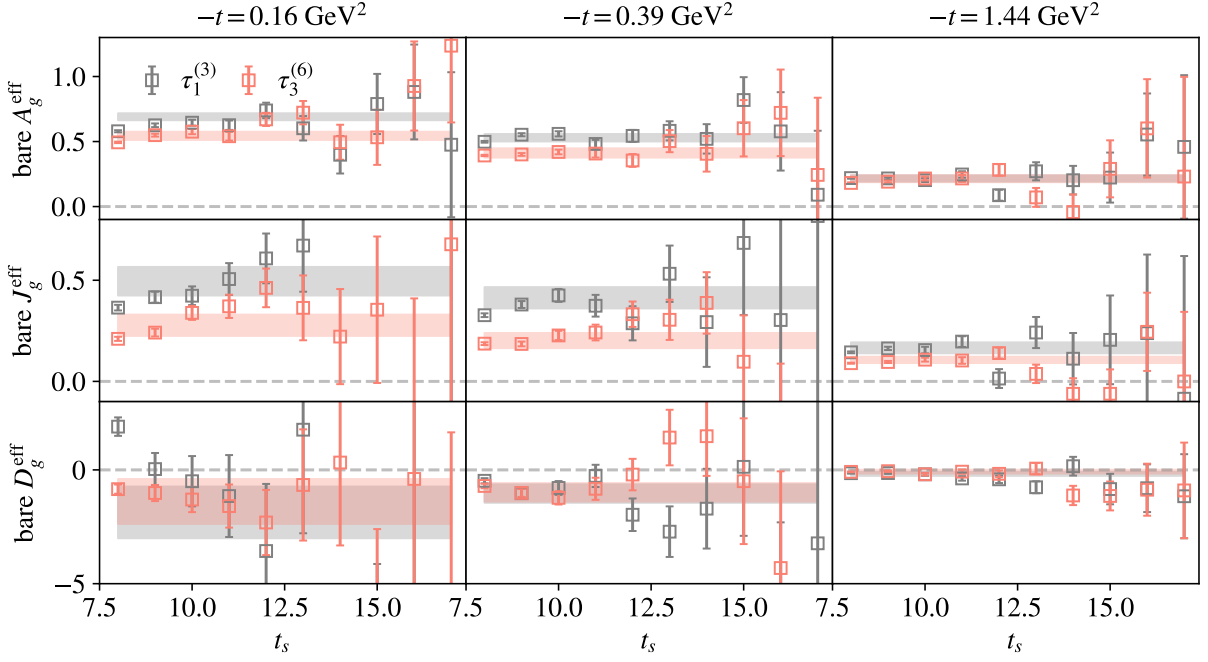
		dipole			z-expansion			
		α	Λ	$\chi^2/$d.o.f	α_0	α_1	α_2	$\chi^2/$d.o.f
A_i	g	0.501(27)	1.262(18)	1.5	0.271(14)	$-0.648(35)$	$-0.089(78)$	1.5
	q	0.510(25)	1.477(44)	0.8	0.314(13)	$-0.591(39)$	$-0.06(13)$	0.8
	v_1	0.1665(56)	1.997(80)	0.7	0.1249(41)	$-0.141(11)$	$-0.029(38)$	0.4
	v_2	0.433(13)	1.524(35)	0.7	0.2768(78)	$-0.493(22)$	$-0.156(77)$	0.6
J_i	g	0.255(13)	1.399(49)	1.1	0.1539(54)	$-0.301(24)$	$-0.26(11)$	1.0
	q	0.251(21)	1.62(13)	0.6	0.1658(85)	$-0.290(42)$	$-0.01(23)$	0.6
	v_1	0.2016(86)	1.698(70)	0.3	0.1399(49)	$-0.219(15)$	$-0.150(68)$	0.3
	v_2	0.222(13)	1.65(10)	0.5	0.1492(61)	$-0.250(26)$	$-0.07(13)$	0.5
D_i	g	$-2.57(84)$	0.538(65)	1.2	$-0.303(28)$	2.20(30)	$-5.2(11)$	1.1
	q	$-1.30(49)$	0.81(14)	0.5	$-0.378(43)$	1.49(45)	$-1.1(17)$	0.6
	v_1	0.009(23)	1.7(50)	0.4	0.0068(83)	$-0.003(54)$	$-0.08(24)$	0.4
	v_2	$-0.77(15)$	0.932(98)	0.9	$-0.272(22)$	1.06(18)	$-1.37(70)$	0.9

TABLE III. Fit parameters of the dipole and z-expansion parametrizations of the t-dependence of the proton GFFs, $A_i(t)$, $J_i(t)$, and $D_i(t)$, renormalized in the $\overline{\text{MS}}$ scheme at scale $\mu = 2$ GeV.
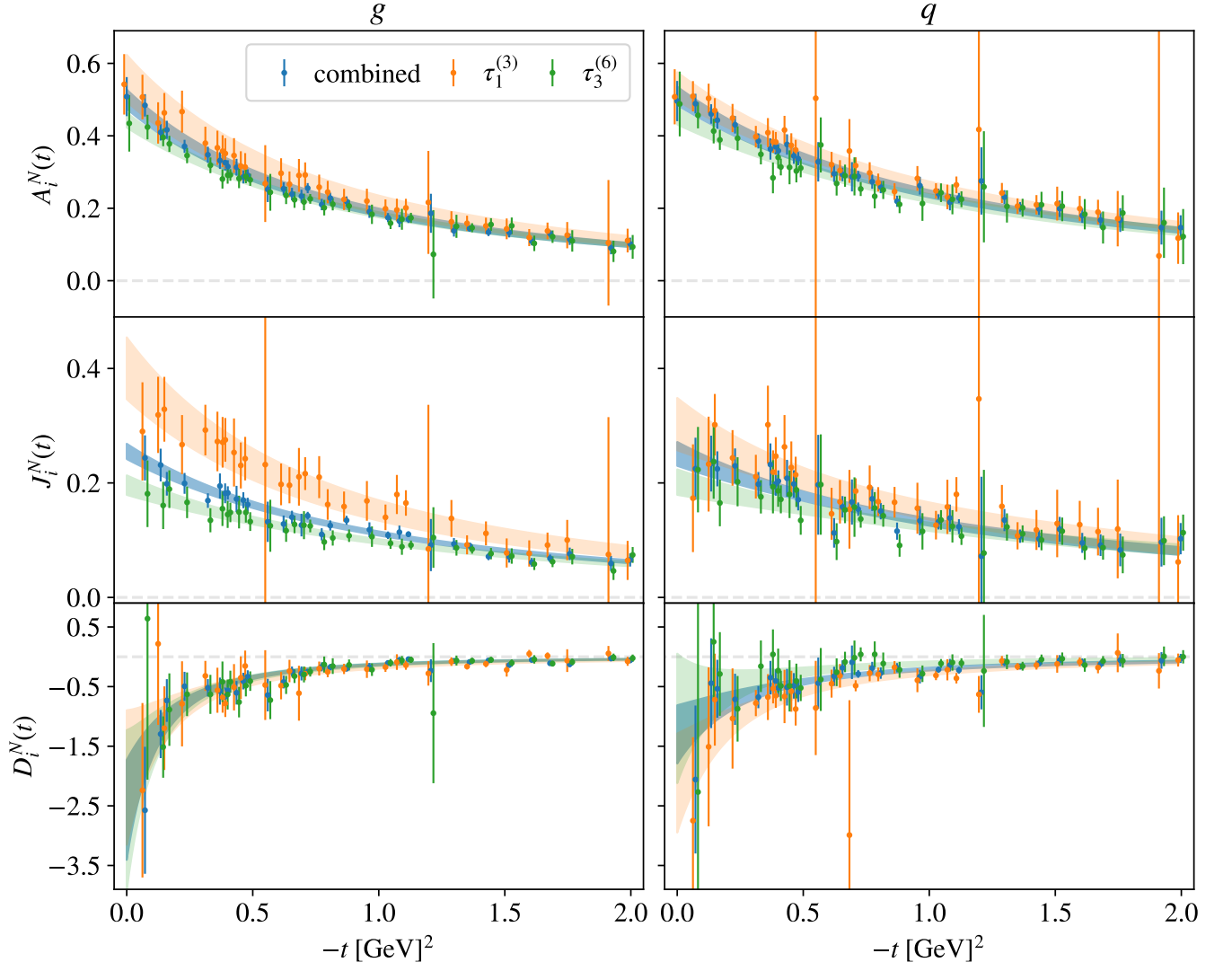
FIG. 12. The renormalized isosinglet quark and gluon combined-irrep GFFs presented in the main text (blue points) shown alongside the GFFs obtained by fitting the results for irrep $\tau_1^{(3)}$ (orange points) or $\tau_3^{(6)}$ (green points) separately. The overlaid bands show dipole fits to the corresponding data.